UC Irvine
UC Irvine Electronic Theses and Dissertations

Title
Compact Laser-Compton X-ray Source Development

Permalink
https://escholarship.org/uc/item/388978k9

Author
Yeh, Po-Chun

Publication Date
2014

Peer reviewed|Thesis/dissertation

UNIVERSITY OF CALIFORNIA,

IRVINE

Compact Laser-Compton X-ray Source Development

THESIS

submitted in partial satisfaction of the requirements
for the degree of

MASTER OF SCIENCE

in Physics

by

Po-Chun Yeh

Thesis Committee:
Professor Peter Taborek, Chair
Professor Toshiki Tajima
Professor Gultekin Gulsen

2014

.

DEDICATION

To

my parents and friends

in recognition of their worth

an apology

A feeling bears on itself the scars of its birth; it recollects as a
subjective
emotion its struggle for existence;
it retains the impress of what might have been, but is not.

Alfred North Whitehead
Process and Reality

and hope

If the fool would persist in his folly he would become wise.

William Blake
"Proverbs of Hell"

TABLE OF CONTENTS

LIST OF FIGURES

ACKNOWLEDGMENTS

Many people have helped me in exercising this work and preparing the thesis, especially I would like to thank my supervisor, Dr. Toshiki Tajima, who guided me throughout each stage in my research work, the discussions and contact made with him had always directed me toward new progress, without his brilliant instruction and great patience, this thesis would be impossible.

In addition, I would like to thank Dr. David J. Gibson, Shawn M. Betts, Dr. Sheldon Wu, Dr. Scott G. Anderson, Dr. Fred V. Hartemann, and Dr. C.P.J. Barty, who provide a lot of resource and help regarding to my research work in Lawrence Livermore National Laboratory

ABSTRACT OF THE THESIS

Compact Laser-Compton X-ray Source Development

By

Po-Chun Yeh

Master of Science in Physics

University of California, Irvine, 2014

Professor Peter Taborek, Chair

The state-of-the-art X-ray source based on inverse-Compton scattering between a high-brightness, relativistic electron beam produced by an X-band RF accelerator and a high-intensity laser pulse generated by chirped-pulse amplification (CPA) has been carried out by our research team at Lawrence Livermore National Laboratory. This system is called "Compact Laser-Compton X-ray Source". The applications include nuclear resonance fluorescence, medical imaging and therapy, and nuclear waste imaging and assay. One of the key factors in this system is how we know the interaction happened in the vacuum chamber, which is the spectrometer of electron beams. The other key factor is the interaction after the spectrometer, which is the outgoing X-ray. In this thesis, the work in the simulation for the result of the interaction between electrons and the laser, the calibration of spectrometer, and laser focus characterization are discussed.

Chapter 1. INTRODUCTION

1-1 Motivation and background

Over the past decades, remarkable technological improvement in the field of high intensity lasers, high-brightness electron linacs, and x-ray diagnostics have contributed to the maturation of a new type of light sources based on Compton scattering, where incident laser photons are scattered by a relativistic electron beam to generate tunable, highly collimated light pulses with picosecond durations, and relatively narrow spectral bandwidth [1].

Furthermore, an increasing number of important applications are being discovered, both experimentally and via detailed computer simulations. In particular, at photon energy below 100 keV, advanced biomedical imaging techniques, including ultrafast x-ray protein crystallography [2], phase contrast imaging [3], and K-edge imaging [4], are under consideration by many groups world-wide. Even though the synchrotron light sources [5] and x-ray free-electron lasers such as LCLS [6] or the European XFEL [7] can provide x-rays with higher brightness in the same energy range, Compton-scattering light sources are more attractive due to their compact footprint. At γ-ray photon energies relevant to nuclear processes and applications, these novel radiation sources will produce the highest peak brilliance. Those applications include nuclear resonance fluorescence (NRF) [8], picosecond positron beams [9], and photo fission.

Recently work has been performed at Lawrence Livermore National Laboratory to show isotope-specific detection of shielded materials via nuclear resonance fluorescence (NRF) using a tunable, quasi-monochromic Compton scattering gamma-ray source. This technique is called Fluorescence Imaging in the Nuclear Domain with Energetic Radiation [10].

This technique has shown extreme promise. There many avenues of research and potential of applications waiting for us to explore.

1-2 Overview

In this thesis, the works including the simulation for the result of the interaction between electrons and the laser, the calibration of the spectrometer, and laser focus characterization will be presented. This work simulates the images detected by the X-ray CCD in order to allow us to predict and verify our experimental data. The input parameters of the electron beam are from PARMELA. We will discuss more detail about how to proceed this simulation. The spectrometer is the vacuum chamber with a magnetic dipole. The interaction between an electron beam and a laser pulse will happen here. Therefore, the calibration of spectrometer is extremely important. We need this calibration for calculation of the electron energy. The laser focus characterization is an important part as well. Since we need an annular beam instead of a Gaussian beam, we have to find out a way to convert the Gaussian beam into Bessel beam and then make annular beam profiles. To achieve this effect, we need some optical methods to simulate the consequence.
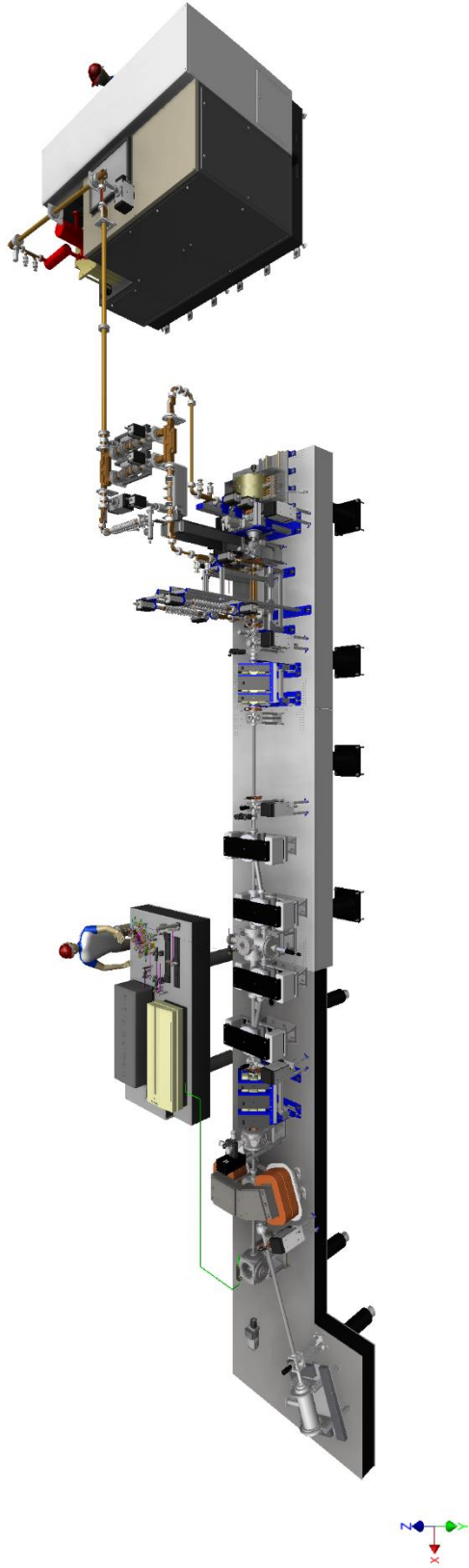
Figure 1. 1 Overview of Compact Laser-Compton X-ray Source

Chapter 2. THEORITICAL CHARATERIZATION OF LASER-COMPTON SCATTERING

2-1 Introduction

While the theory of Compton backscattered radiation is well-established, there remains a need to have a complete three-dimensional time resolved computational capability for the full determination of the temporally and spatially resolved spectra and intensity distributions produced by a Compton-scattering interaction of arbitrary geometry. This capability is very critical for our design of Compton-scattering x-ray sources and further experiments and applications utilizing such techniques. In this chapter, we present a newly developed fully three-dimensional time and frequency-domain code used for calculations of Compton backscattering of a short and intensive laser pulse with a relativistic electron beam. This is achieved by applying Compton-scattering differential cross section and appropriate Lorentz transformations. The 3D code developed using this method was designed to enhance existing computational capabilities, namely, a 3D frequency-domain code developed by Hartemann *et al.* [11]. Therefore, we continued improving the computational method for various uses.

This work simulates the images detected by the X-ray CCD in order to allow us to predict and verify our experimental data. The input parameters of the electron beam are from PARMELA [12].

2-2 Compton scattering

Compton backscattered photons are generated when an electron beam collides with a photon beam (i.e., laser). In the limit, the incident photon has a very small energy compared to the electron rest mass, and therefore, the scattered photon has the same energy as the incident photon in the electron rest frame. The brightness of Compton-scattering light sources has been studied theoretically and computationally.
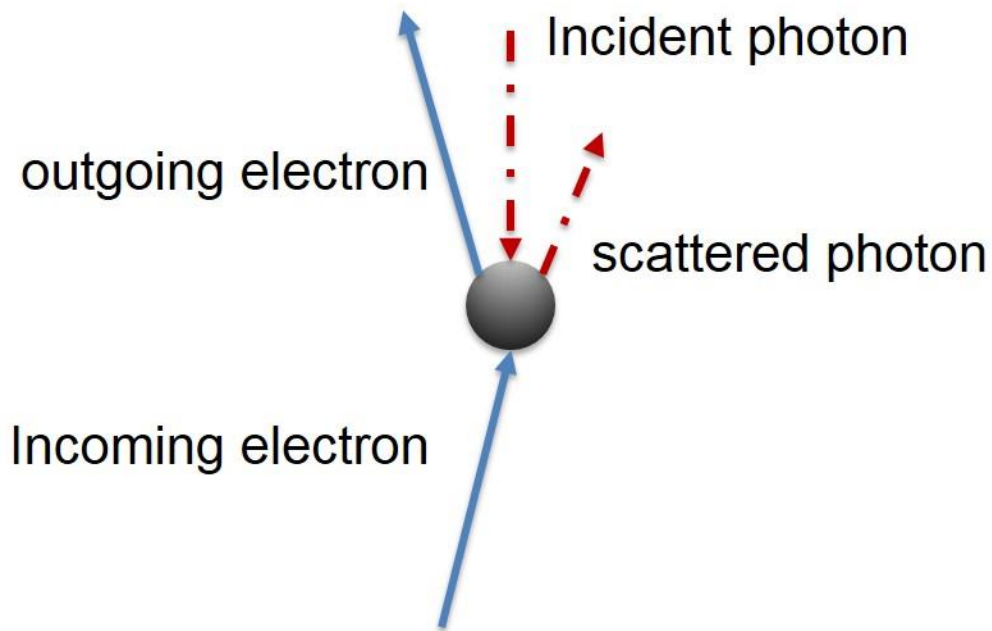
Figure 2. 1 Schematic of Compton scattering.

2-2-1   4-vectors in the system

All units in this section: the length is measured in units of the electron reduced Compton wavelength, $\lambdabar = \dfrac{\hbar}{m_0 c}$; the time in units of $\dfrac{\lambdabar}{c}$; the mass in

units of the electron rest mass, m_0; and charge in units of e. Also, $\varepsilon_0 = \frac{1}{4}\pi\alpha$, where α is the fine structure constant.

In the linear regime, the total number of scattered photons could be shown in terms of the scattering cross-section, σ; 4-current density, j^μ; and incident photon 4-flux, Φ^μ:

$$N_x = \int \sigma j_\mu \Phi^\mu d^4 x; \quad j^\mu = n_e \frac{u^\mu}{\gamma}; \quad \Phi^\mu = n_\lambda \frac{k^\mu}{k};$$
$$N_x = \sigma \int n_e n_\lambda \frac{k_\mu u^\mu}{k\gamma} d^4 x. \tag{1}$$

Here, n_e and n_λ represent the electron beam and incident photon densities, respectively; $k^\mu = (\frac{\omega_0}{c}, \mathbf{k}_0)$ is the incident 4-wavenumber; and $u^\mu = (\gamma, \mathbf{u})$ is the initial electron 4-velocity. The term $\frac{k_\mu u^\mu}{k\gamma}$ represents the relative velocity.

For an electron, the density is replaced by the product of three Dirac delta-distributions:

$$N_x = \sigma \frac{k_\mu u^\mu}{k\gamma} \int n_\lambda \delta[\mathbf{x} - \mathbf{r}(t)] d^4 x = \sigma \frac{k_\mu u^\mu}{k\gamma} \int_{-\infty}^{+\infty} n_\lambda [\mathbf{r}(t), t] dt. \tag{2}$$

We are assuming that the 4-velocity is independent of space or time, which corresponds to ballistic trajectories: $r^\mu(\tau) = [t(\tau), \mathbf{r}(\tau)] = r_0^\mu + u^\mu \tau$. Physically, this implies that the oscillation amplitude is small compared to the laser wavelength, so that the electron trajectory remains essentially inertial.

The number of photons scattered per unit frequency and solid angle can be obtained by the differentiation [13] [14] [15]:

$$\frac{d^2 N_x}{dq d\Omega} = \frac{d^2 \sigma}{dq d\Omega} \frac{k_\mu u^\mu}{k\gamma} \int_{-\infty}^{+\infty} n_\lambda(t) dt. \tag{3}$$

where the scattered 4-wavenumber is represented by $q^\mu = q(1, \sin\theta\cos\varphi, \sin\theta\sin\varphi, \cos\theta)$, in the spherical coordinates. We will discuss that later.

2-2-2   Differential scattering cross section

The Klein-Nishina differential scattering cross section derived by Ref. [16] and Ref. [17]:

$$\frac{d^2\sigma}{dq d\Omega} = \frac{\alpha^2}{2} \frac{q}{\kappa} \delta(\kappa - \lambda - \mu) X;$$

$$X = \frac{1}{2}\left(\frac{\kappa}{\lambda} + \frac{\lambda}{\kappa}\right) - 1 + 2\left[\varepsilon^\mu \pi_\mu - \frac{(\varepsilon^\mu u_\mu)(\pi^\nu v_\nu)}{\kappa} + \frac{(\varepsilon^\mu v_\mu)(\pi^\nu u_\nu)}{\lambda}\right]^2. \tag{4}$$

In these equations, q is the scattered 4-wavenumber, q^μ; κ and λ are the incident and scattered light-cone variables; μ is the recoil parameter; ε^μ and π^μ are the incident and scattered 4-polarizations; finally, u^μ and v^μ are the initial and final electron 4-velocities. These quantities are defined as follows:

$$\kappa = k^\mu u_\mu; \quad \lambda = q^\mu u_\mu; \quad \mu = k^\mu q_\mu;$$
$$v^\mu = u^\mu + k^\mu - q^\mu. \tag{5}$$

2-2-3   4-polarizations

The incident 4-polarization corresponds to the direction of oscillation of the electron subjected to the Lorentz force:

$$\frac{du_\mu}{d\tau} = F_{\mu\nu}u^\nu = \left(\partial_\mu A_\nu - \partial_\nu A_\mu\right)u^\nu; \tag{6}$$

where the incident plane wave radiation field derives from the 4-potential;

$$A_\mu = \sigma_\mu A_0 e^{i\phi}; \quad \phi = k_\mu x^\mu; \quad F_{\mu\nu} = iA_0 e^{i\phi}\left(\sigma_\mu k_\nu - \sigma_\nu k_\mu\right). \tag{7}$$

The electron dynamics is described by:

$$\frac{du_\mu}{d\tau} = iA_0 e^{i\phi}\left[\sigma_\mu\left(k_\nu u^\nu\right) - k_\mu\left(\sigma_\nu u^\nu\right)\right]. \tag{8}$$

This equation can be solved by projection:

$$k^\mu \frac{du_\mu}{d\tau} = \frac{d}{d\tau}\left(k^\mu u_\mu\right) = iA_0 e^{i\phi}\left[\left(k^\mu \sigma_\mu\right)\left(k_\nu u^\nu\right) - \left(k^\mu k_\mu\right)\left(\sigma_\nu u^\nu\right)\right] = 0;$$

$$\sigma^\mu \frac{du_\mu}{d\tau} = \frac{d}{d\tau}\left(\sigma^\mu u_\mu\right) = iA_0 e^{i\phi}\left[\left(\sigma^\mu \sigma_\mu\right)\left(k_\nu u^\nu\right) - \left(\sigma^\mu k_\mu\right)\left(\sigma_\nu u^\nu\right)\right] = -i\kappa A_0 e^{i\phi}. \tag{9}$$

In fact, the Lorentz gauge condition, $\partial_\mu A^\mu = 0$, requires that $k_\mu \sigma^\mu = 0$; while the dispersion relation *in vacuum* is $k_\mu k^\mu = 0$. In addition, since the 4-velocity is normalized, with $u_\mu u^\mu = 1$; $u^\mu \frac{du_\mu}{d\tau} = 0$. The first line in Equation (9) shows that the incident light-cone variable is a constant of motion: $\kappa = \kappa_0 = k_\mu u_0^\mu$, where u_μ^0 is the electron initial momentum. The second line yields the evolution of the transverse momentum:

$$\kappa = k_{\mu} u^{\mu} = k_{\mu} \frac{dx^{\mu}}{d\tau} = \frac{d\phi}{d\tau};$$

$$\frac{d}{d\tau}\left(\sigma^{\mu} u_{\mu} + A_0 e^{i\phi}\right) = 0 \qquad (10)$$

Hence, we seek a solution of the form:

$$u_{\mu}(\phi) = a(\phi) u_{\mu}^{0} + b(\phi)\sigma_{\mu} + c(\phi) k_{\mu}. \qquad (11)$$

Projecting Equation (11) along the 4-wavenumber, we find that:

$$\kappa = a(\phi) k^{\mu} u_{\mu}^{0} = a(\phi)\kappa_0; \quad a(\phi) = 1. \qquad (12)$$

The projection along the incident 4-potential yields:

$$\sigma^{\mu} u_{\mu}(\phi) = \sigma^{\mu} u_{\mu}^{0} - b(\phi);$$

$$\frac{d}{d\tau}\left(\sigma^{\mu} u_{\mu} + A_0 e^{i\phi}\right) = 0 = \frac{d}{d\tau}\left[A_0 e^{i\phi} - b(\phi)\right]; \qquad (13)$$

$$b(\phi) = A_0 e^{i\phi}.$$

Eventually, the normalization requires that

$$u_{\mu} u^{\mu} = 1 = \left(u_{\mu}^{0} + b\sigma_{\mu} + c k_{\mu}\right)\left(u_0^{\mu} + b\sigma^{\mu} + c k^{\mu}\right);$$

$$= u_{\mu}^{0} u_0^{\mu} - b^2 + 2bu_{\mu}^{0}\sigma^{\mu} + 2c k_{\mu} u_0^{\mu}; \qquad (14)$$

$$= 1 - b^2 + 2bu_{\mu}^{0}\sigma^{\mu} + 2c\kappa_0.$$

Solving Equation (14) for c, we can obtain:

$$c(\phi) = \frac{A_0^2 e^{2i\phi} - 2A_0 e^{i\phi}\sigma^{\mu} u_0^{\mu}}{2\kappa_0} = -\frac{A_{\mu}\left(A^{\mu} + 2u_0^{\mu}\right)}{2\kappa_0};$$

$$u_{\mu} = u_{\mu}^{0} + A_{\mu} - k_{\mu}\frac{A_{\nu}\left(A^{\nu} + 2u_0^{\nu}\right)}{2\kappa_0}. \qquad (15)$$

In the limit of vanishingly small excitations ($A_0 \rightarrow 0$),

$$u_\mu \simeq u_\mu^0 + A_0 e^{i\phi}\left(\sigma_\mu - k_\mu \frac{\sigma_\nu u_0^\nu}{\kappa_0}\right) = u_\mu^0 + \varepsilon_\mu A_0 e^{i\phi}; \qquad (16)$$

which defines the incident 4-polarization, ε_μ.

Equation (5) can be simplified by using the following properties of the incident 4-polarization:

$$\varepsilon^\mu = \sigma^\mu - k^\mu \frac{\sigma^\nu u_\nu}{\kappa}; \quad \sigma^\mu = \frac{A^\mu}{\sqrt{-A^\nu A_\nu}};$$

$$\sigma^\mu \sigma_\mu = -1; \quad \sigma^\mu k_\mu = 0; \qquad (17)$$

$$\varepsilon^\mu \varepsilon_\mu = -1; \quad \varepsilon^\mu k_\mu = 0; \quad \varepsilon^\mu u_\mu = 0;$$

Now we have: $\varepsilon^\mu v_\mu = \varepsilon^\mu\left(u_\mu + k_\mu - q_\mu\right) = -\varepsilon^\mu q_\mu$, and

$$\frac{d^2\sigma}{dq d\Omega} = \frac{\alpha^2}{2}\frac{q}{\kappa}\delta\left(\kappa - \lambda - \mu\right)\left(Q + D\right);$$

$$Q = \frac{\left(\kappa - \lambda\right)^2}{2\kappa\lambda}; \quad D = 2\left[\varepsilon^\mu \pi_\mu - \frac{\left(\varepsilon^\mu q_\mu\right)\left(\pi^\nu u_\nu\right)}{\lambda}\right]^2. \qquad (18)$$

Here, the angular components of the cross section have been labeled *Q* for the QED phase space correction, and *D* for the classical dipole component. In situations when there is no need to distinguish between the initial and dynamic 4-velocities, we drop the 0 subscript and write u_μ.

The scattered 4-polarization can be defined by using the Liénard-Wiechert 4-potentials,

$$B_\mu^\pm = \alpha \left. \frac{u_\mu}{\left| u_\nu (x-r)^\nu \right|} \right|_{\tau^\pm} ; \tag{19}$$

where the retarded and advanced 4-potentials are determined by the appropriate pole:

$$\left[x - r(\tau_\pm) \right]^2 = 0; \quad r^0(\tau_\pm) \gtrless x^0 \tag{20}$$

Here, $r^\mu(\tau)$ is the electron 4-trajectory, and $u^\mu(\tau) = \dfrac{dr^\mu(\tau)}{d\tau}$.

Introducing the distance between the point of observation and the electron at the retarded proper time, R, we can recast Equation (19) as follows:

$$B_\mu^- = \alpha \left. \frac{u_\mu}{\left| u_\nu R \dfrac{q^\nu}{q} \right|} \right|_{\tau^-} ; \tag{21}$$

where $q^\mu / q = (1, \hat{\mathbf{n}})$, and $\hat{\mathbf{n}}$ is the direction of observation.

For our need, with $A_0 \ll 1$, we have:

$$B_\mu^- \simeq \alpha \left. \frac{u_\mu^0 + \varepsilon_\mu A_0 e^{i\phi}}{\left| \dfrac{R}{q} \left(u_\nu^0 + \varepsilon_\nu A_0 e^{i\phi} \right) q^\nu \right|} \right|_{\tau^-} \simeq \alpha \left. \frac{\left(u_\mu^0 + \varepsilon_\mu A_0 e^{i\phi} \right) \left(1 - \dfrac{\varepsilon_\nu q^\nu}{u_\lambda^0 q^\lambda} A_0 e^{i\phi} \right)}{\left| \dfrac{R}{q} u_\nu^0 q^\nu \right|} \right|_{\tau^-} . \tag{22}$$

Keeping the linear oscillatory term only, we define the scattered 4-polarization as follows:

$$\pi_\mu = \eta \left(\varepsilon_\mu - u_\mu^0 \frac{\varepsilon_\nu q^\nu}{u_\lambda^0 q^\lambda} \right) A_0 e^{i\phi}; \qquad (23)$$

where η is a normalization constant, such that $\pi_\mu \pi^\mu = -1$. Using the fact that $\varepsilon_\mu \varepsilon^\mu = -1$, $\varepsilon_\mu u^\mu = 0$, $u_\mu u^\mu = 1$, and $u_\mu q^\mu = \lambda$; the result is:

$$\pi_\mu = \frac{\varepsilon_\mu - u_\mu \dfrac{\varepsilon_\nu q^\nu}{\lambda}}{\sqrt{1 - \left(\dfrac{\varepsilon_\lambda q^\lambda}{\lambda} \right)^2}}. \qquad (24)$$

We note that, as expected from transversality, $\pi_\mu q^\mu = 0$.

In the end, the dipole component of the differential scattering cross section can be written in a much more compact form:

$$D = 2\left[\pi_\mu \left(\varepsilon^\mu - u^\mu \frac{\varepsilon_\nu q^\nu}{\lambda} \right) \right]^2 = 2\left(\pi_\mu \pi^\mu \sqrt{1 - \left(\frac{\varepsilon_\nu q^\nu}{\lambda} \right)^2} \right)^2 = 2\left[1 - \left(\frac{\varepsilon_\mu q^\mu}{\lambda} \right)^2 \right] \quad (25)$$

2-2-4   Spherical coordinates

For our need, we define the incident 4-wavenumber, initial electron 4-velocity, and scattered 4-wavenumber in spherical coordinates:

$$k^\mu = k(1,0,0,-1);$$
$$u^\mu = (\cosh \rho, \sinh \rho \sin \varepsilon \cos \phi, \sinh \rho \sin \varepsilon \sin \phi, \sinh \rho \cos \varepsilon); \quad (26)$$
$$q^\mu = q(1, \sin \theta \cos \varphi, \sin \theta \sin \varphi, \cos \theta).$$

The incident radiation propagates along the negative z-axis; ρ is the electron rapidity.

The incident and scattered light-cone variables, and the recoil parameter will become:

$$\kappa = k\left(\cosh\rho + \cos\varepsilon\sinh\rho\right);$$
$$\lambda = q\left\{\cosh\rho - \sinh\rho\left[\cos\varepsilon\cos\theta + \sin\varepsilon\sin\theta\cos\left(\phi-\varphi\right)\right]\right\};\quad(27)$$
$$\mu = kq\left(1+\cos\theta\right).$$

2-2-5   Dose

In order to calculate the spectral distribution yielded by the interaction, which has to take into account several other parameters. The most useful expression to describe the source is typically the local differential brightness, which can be obtained from the local number of photons scattered per unit time and volume [18]

$$\frac{d^{12}N}{d^4x\,dq\,d\Omega\,d^3u\,d^3k} = \frac{d\sigma}{d\Omega}\delta(q-q_c)\frac{d^3n_e}{d^3u}\frac{d^3n_\lambda}{d^3k}\frac{u_\mu k^\mu}{\gamma k},\quad(28)$$

where $\dfrac{d^3n_e}{d^3u}$ and $\dfrac{d^3n_\lambda}{d^3k}$ represent the electron beam phase space density and laser pulse momentum space density.

To simplify the calculation, calculating the total integrated number of γ-ray photons is way to go. As derived in Ref. [19], the temporal behavior of the γ-ray pulse can be described in Cartesian coordinates:

$$\frac{d^3N}{2\pi r\,dr\,dz\,c\,dt} = \sigma(1+\beta_0)n_\lambda(\mathrm{r,z,t})n_e(\mathrm{r,z,t}).\quad(29)$$

where $n_e(\mathrm{r}, \mathrm{z}, \mathrm{t})$ is the incident electron beam density and $\sigma = \dfrac{8\pi r_0^2}{3}$ is the Compton-scattering cross section. To evaluate the dose yielded by only one macroparticle (i.e., an electron) along its trajectory (r_e, z_e), which can substitute $n_e(\mathrm{r}, \mathrm{z}, \mathrm{t})$ by $\delta(r = r_e, z = z_e, \mathrm{t})$ to end with

$$
\begin{aligned}
\frac{d^3 N}{cdt} &= \sigma(1 + \beta_0) n_\lambda(\mathrm{r}, \mathrm{z}, \mathrm{t}) \delta(r = r_e, z = z_e, \mathrm{t}) \\
&= \sigma(1 + \beta_0) n_\lambda(r = r_e, z = z_e, \mathrm{t})
\end{aligned}
\tag{30}
$$

In other words,

$$
\begin{aligned}
N_i &= \sigma(1 + \beta_0) \frac{N_\lambda}{\sqrt{\pi/2} w_0^2 c \Delta t 3} \int_{-\infty}^{\infty} \frac{1}{1 + \bar{z}^2} \\
&\times \exp[-2(\frac{z_0}{c\Delta t})^2 (\bar{\mathrm{t}} - \bar{z})^2 - 2\frac{\bar{r}^2}{1 + \bar{z}^2}] d\bar{\mathrm{t}},
\end{aligned}
\tag{31}
$$

To evaluate this integral, we can use the electron's ballistic trajectories, as defined below.

$$
x(\mathrm{t}) = \mathrm{x}_0 + \frac{u_x}{\gamma} ct, \quad \mathrm{y}(\mathrm{t}) = y_0 + \frac{u_y}{\gamma} ct
$$

$$
\mathrm{z}(\mathrm{t}) = z_0 + \frac{u_z}{\gamma} ct, \quad r^2(t) = x^2(t) + y^2(t)
\tag{32}
$$

The total dose is then simply obtained by summing over all the macroparticles, and by taking into account the ratio N_e/n between the total number of electrons in the beam and macroparticles in the code.

2-3 Models made with PARMELA

These models of electrons are based on the simulation data of PARMELA, which is developed by UCLA PBPL. PAMELA is a 3D particle tracker to simulate the dynamic motion in RF injector beam lines. It includes space charge and image charge routines. It covers many analytic expressions of beam line components such as RF cavities, solenoid magnets, and dipole and quadrupole magnets. We specifically use this as our source for the simulation.

To model the distribution of electron, it is important to understand the distribution of energies with phases. Different electrons are ejected by different energies and phases. It is the profile showing the quality of the out coming electrons from the injector. The balletic trajectory needs to consider the phases. We can also use the electron's ballistic trajectories to animate their dynamic motions.

$$x(\mathrm{t}) = \mathrm{x}_0 + \frac{u_x}{\gamma} ct, \mathrm{y}(\mathrm{t}) = y_0 + \frac{u_y}{\gamma} ct$$

$$\mathrm{z}(\mathrm{t}) = z_0 + \frac{u_z}{\gamma} ct, r^2(t) = x^2(t) + y^2(t)$$

(33)

The PARMELA output formats are : x (cm), θ_x (mrad), y (cm), θ_y (mrad), ϕ (degree) , W (MeV), #, where θ_x and θ_y are differentiated x and y by z, respectively, ϕ is a phase of energy, and W is an energy of electron. The profiles of them will be presented below.
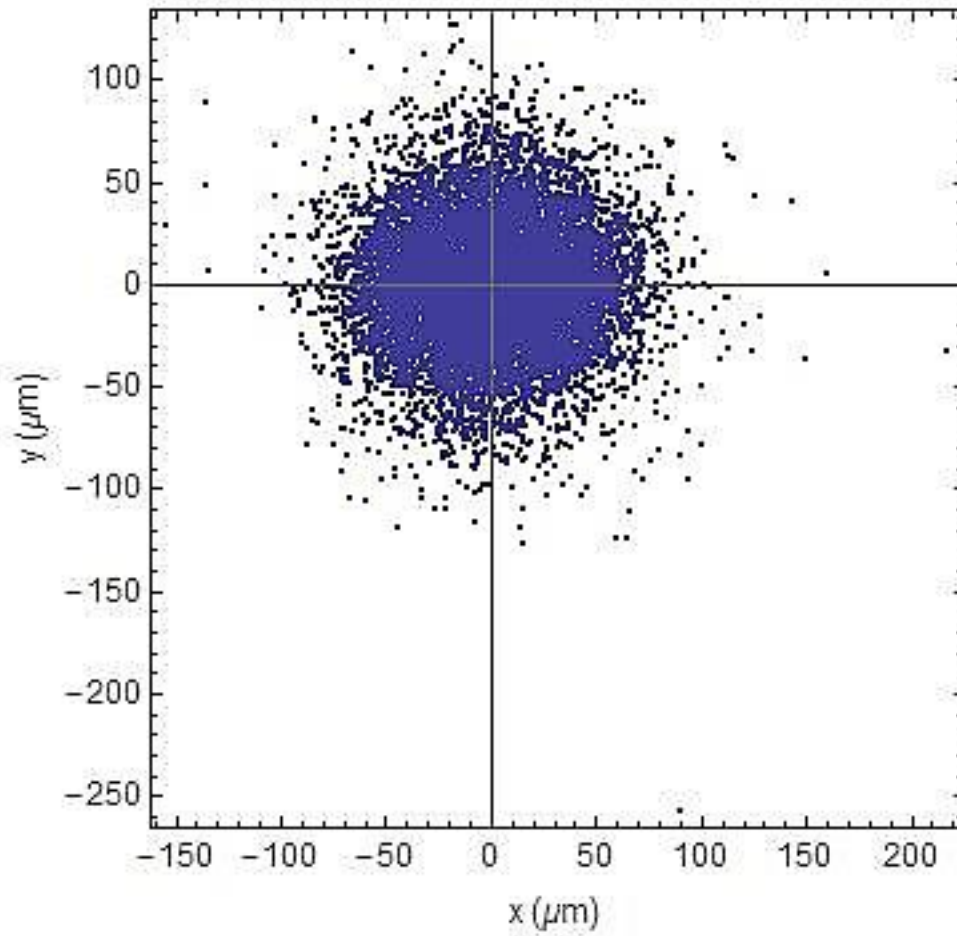
Figure 2. 2 The plot of y-position versus x-position for all electrons from PARMELA.
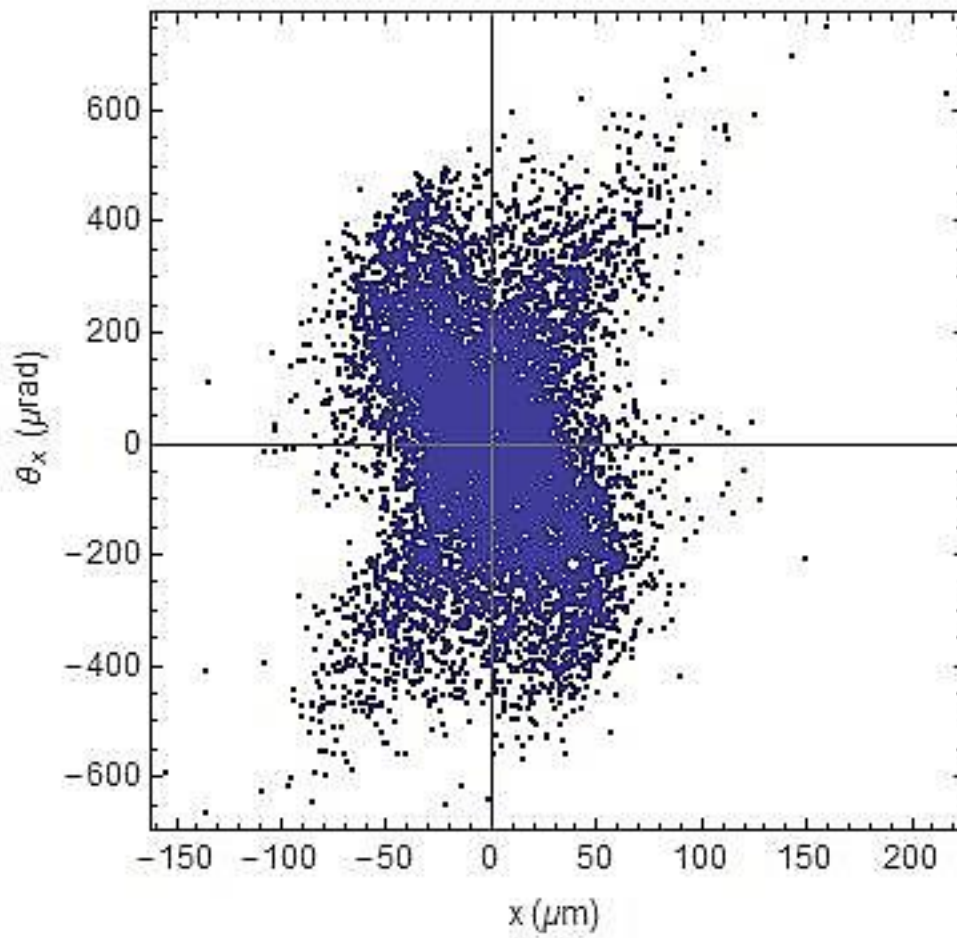
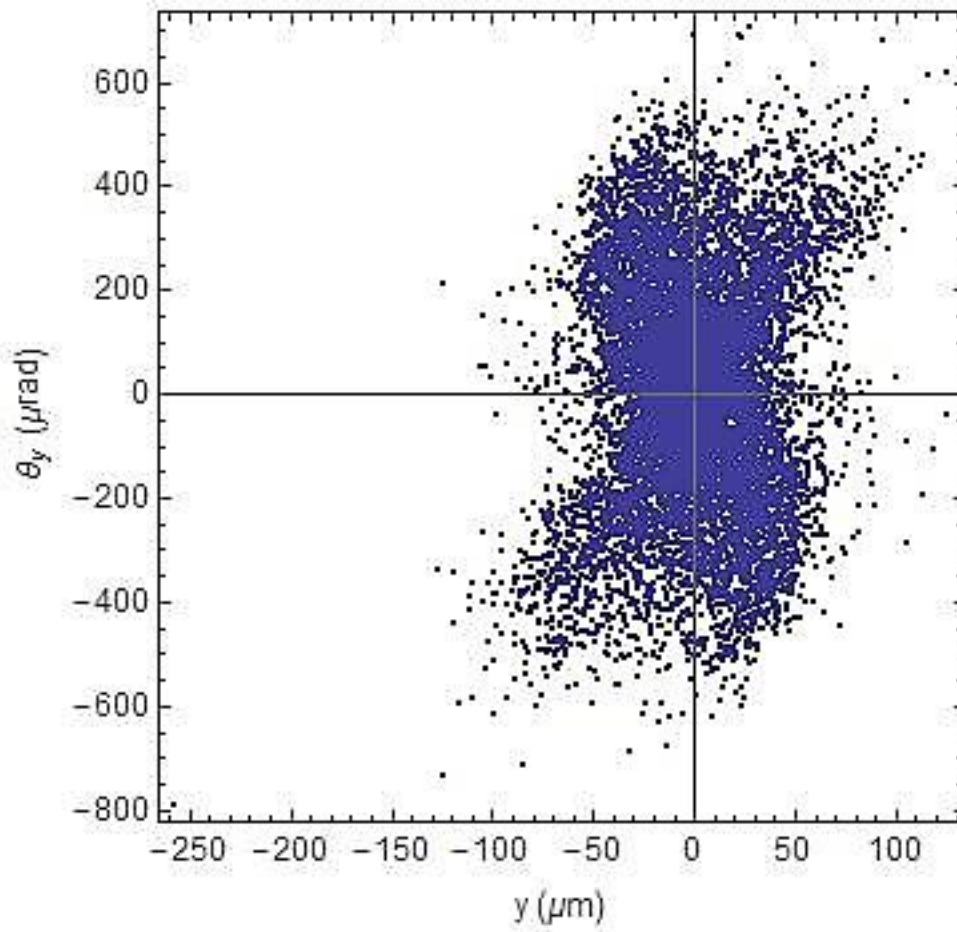**Figure 2. 3** The plot of θ_x versus x-position for all electrons from PARMELA.

Figure 2. 4 The plot of θ_y versus y-position for all electrons from PARMELA.
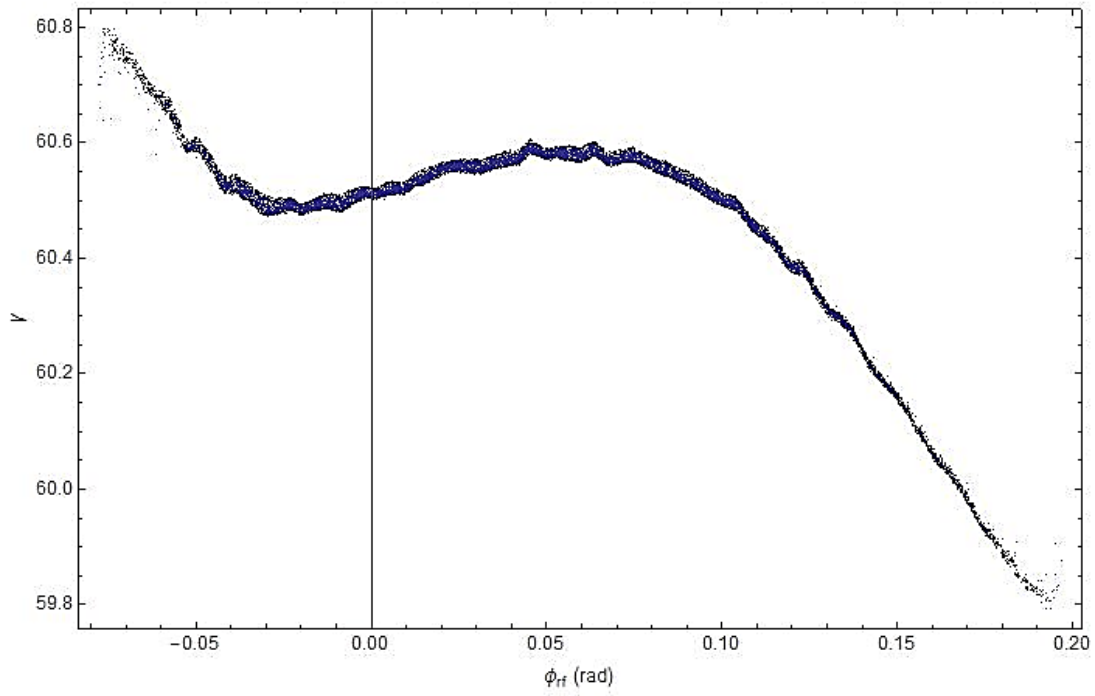
Figure 2. 5 The plot of energy versus phase for all electrons from PARMELA.
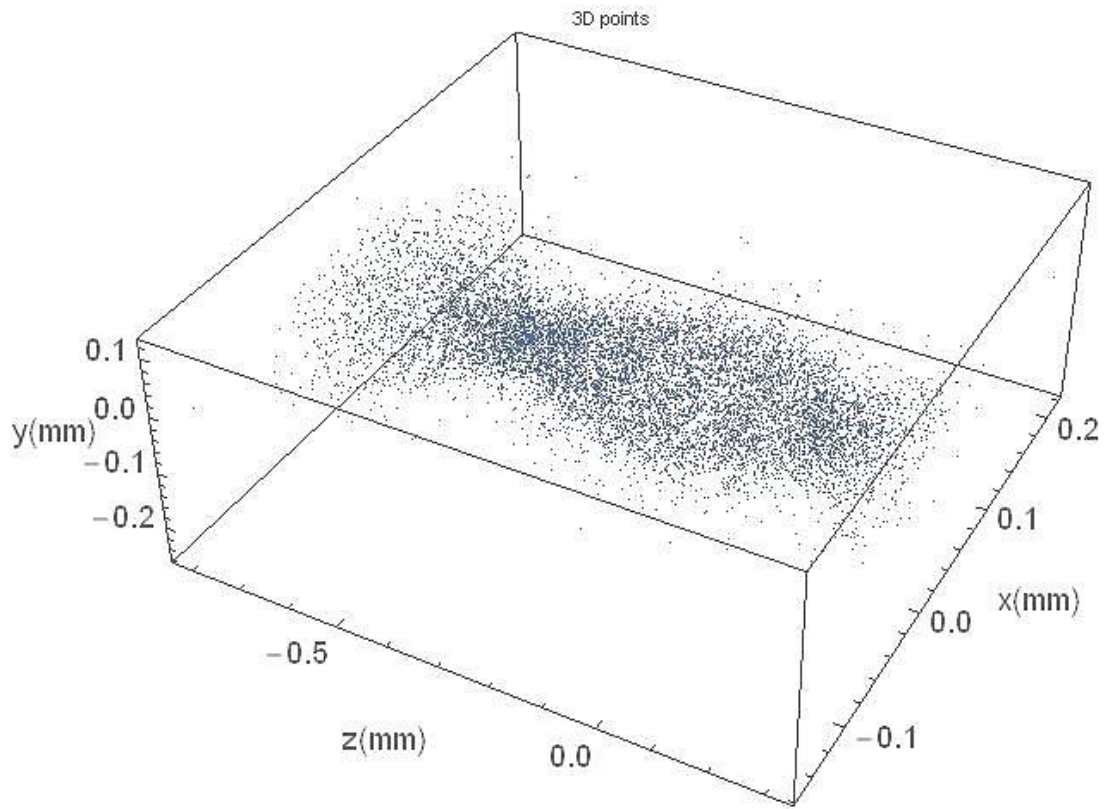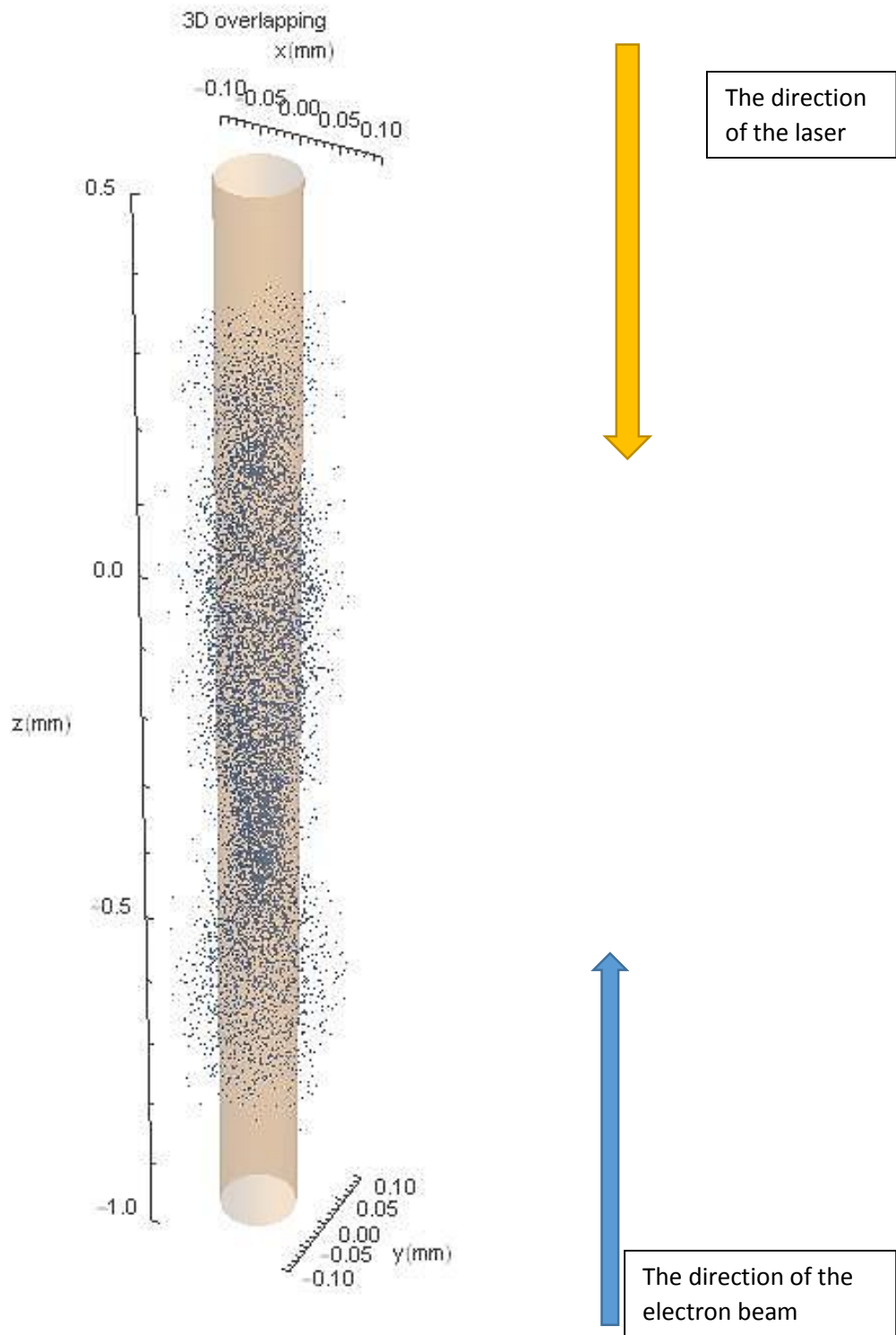
Figure 2. 6 The spatial distribution of all electrons propagating along with the z-axis from PARMELA.

3D overlapping

x(mm)

The direction
of the laser

The direction of the
electron beam

Figure 2. 7 The spatial distribution of all electrons propagating along with the z-axis from PARMELA overlapping the laser focus shown by the yellow cylinder.

2-4 Gaussian modes

To simplify the simulation, we first look into the Gaussian beam instead of the Bessel beam, because the Gaussian beam is more trivial.

The useful mathematical expression is

$$E(r,z) = E_0 \frac{w_0}{w(z)} \exp\left(\frac{-r^2}{w(z)} - ikz - ik\frac{r^2}{2R(z)} \right),$$

where r is the radial distance from the center axis of the beam, z is the axial distance from the beam's narrowest point (the "waist"), k is the wavevector, $w(z)$ is the radius at which the field amplitude and intensity drop to $1/e$ and $1/e^2$ of their axial values, respectively, and $R(z)$ is the radius of curvature of the beam's wavefronts.

In addition, $w(z)$ is defined as

$$w(z) = w_0 \sqrt{1 + \left(\frac{z}{z_R} \right)^2}$$

$$z_R = \frac{\pi w_0^2}{\lambda}$$

where z_R is called Rayleigh range.
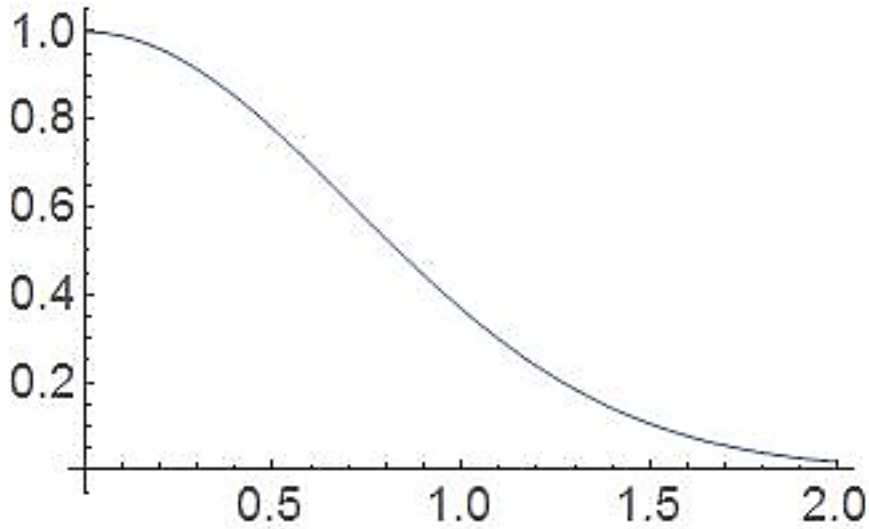
Figure 2. 8 An example of Gaussian beam.

As the simulation of Gaussian modes is a quite matured approach in this field, we will discuss more in this section. All data is retrieved from PARMELA.

2-4-1　　Dose

From the distributions of doses, we can find how the electrons interact with the incoming photons (i.e., laser). Higher doses mean that the interactions between electrons and photons are better. From the histogram, we can find out how many particles contributing certain doses. It is also important to know the distribution in order to see how the particles distribute.
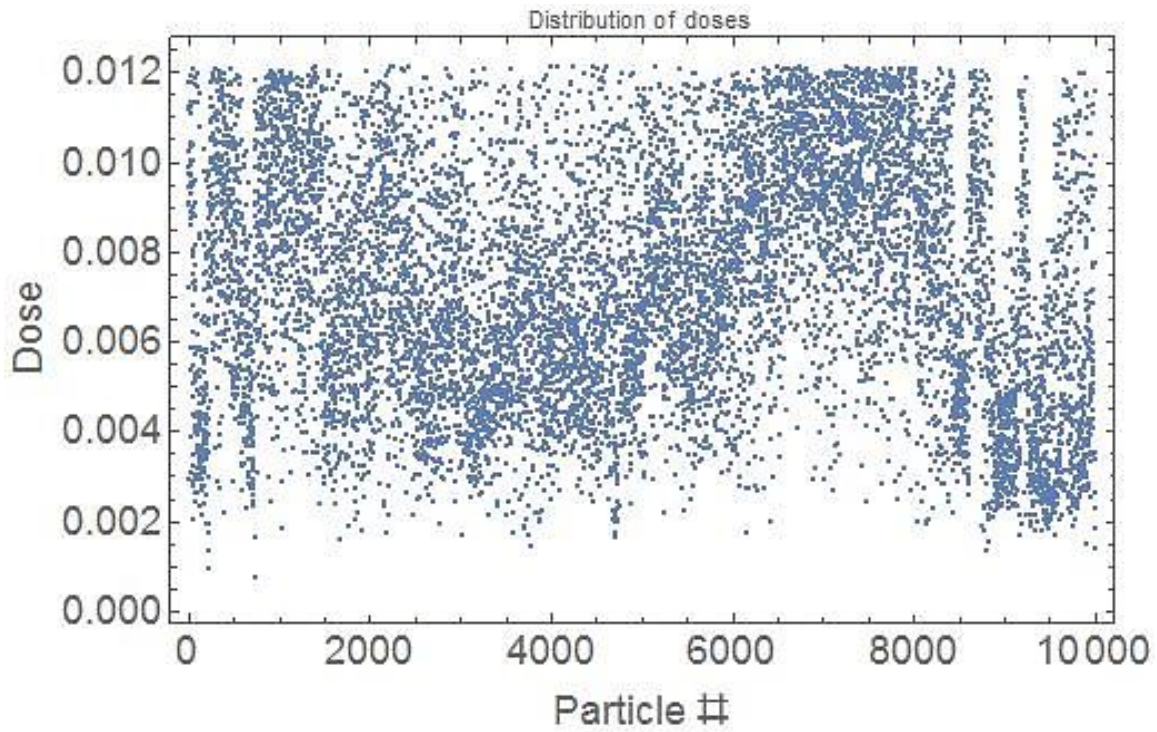
Figure 2. 9 Distribution of doses from PARMELA.

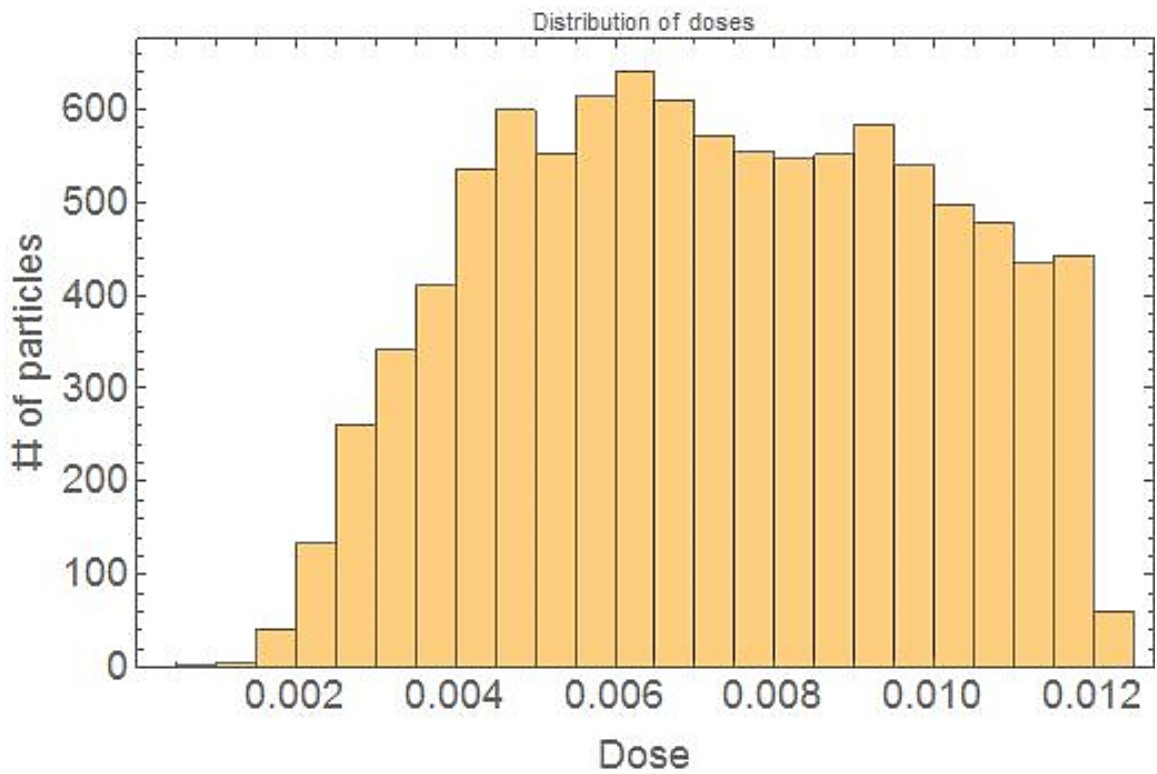**Figure 2. 10** Histogram of Distribution of doses from PARMELA

To optimize the dose, one is important to find a suitable laser focal spot. Thus, we write another code to process our need.
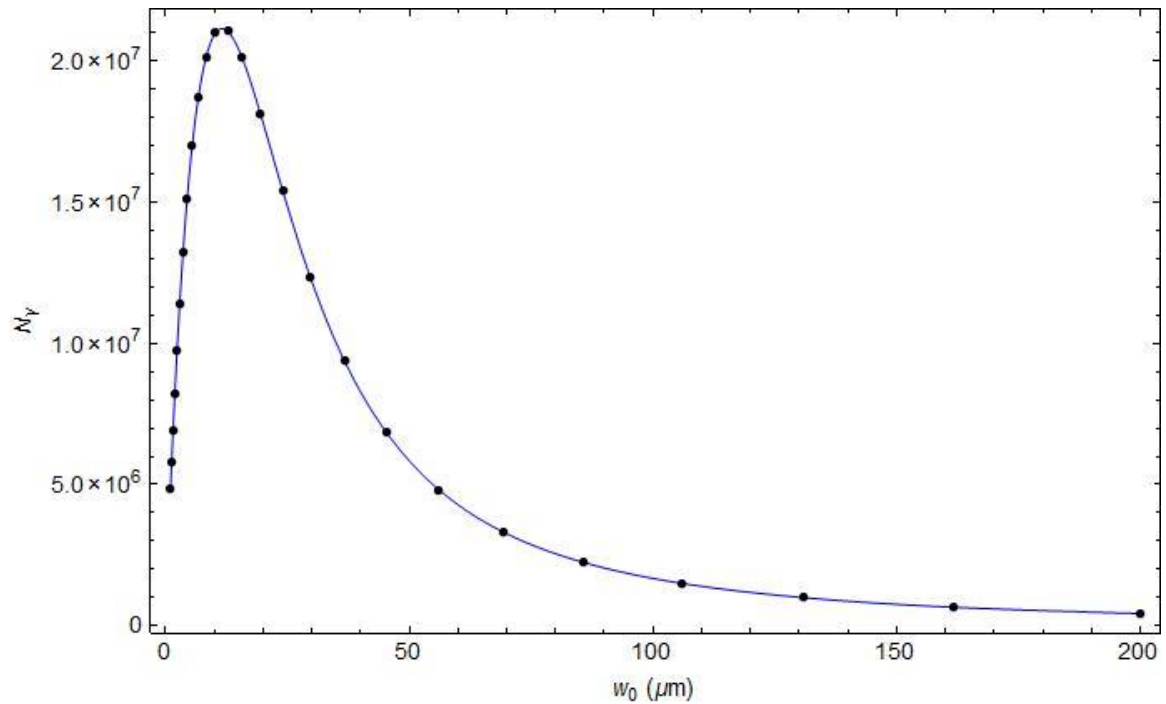
Figure 2. 11 An example for finding a suitable focal spot size for the maximum dose (the vertical axis is the number of photons and the horizontal one is the sizes of the focal spots).
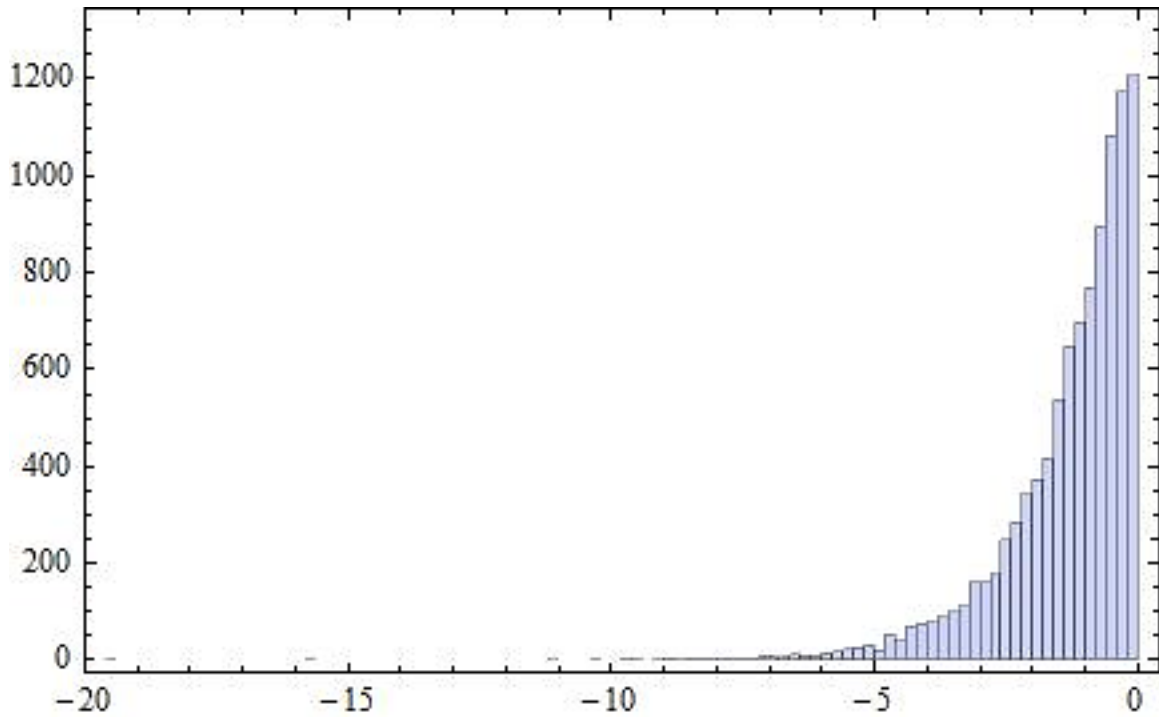
Figure 2. 12 Histogram of all maximum doses of electrons (the horizontal axis shows the difference from the maximum doses).

2-4-2 X-ray image simulation

In this section, we will discuss cases for unpolarized and X-polarized lasers with the energy responses of materials and overlapping. The overlapping means that the images simulated do include the integrated doses of electrons.
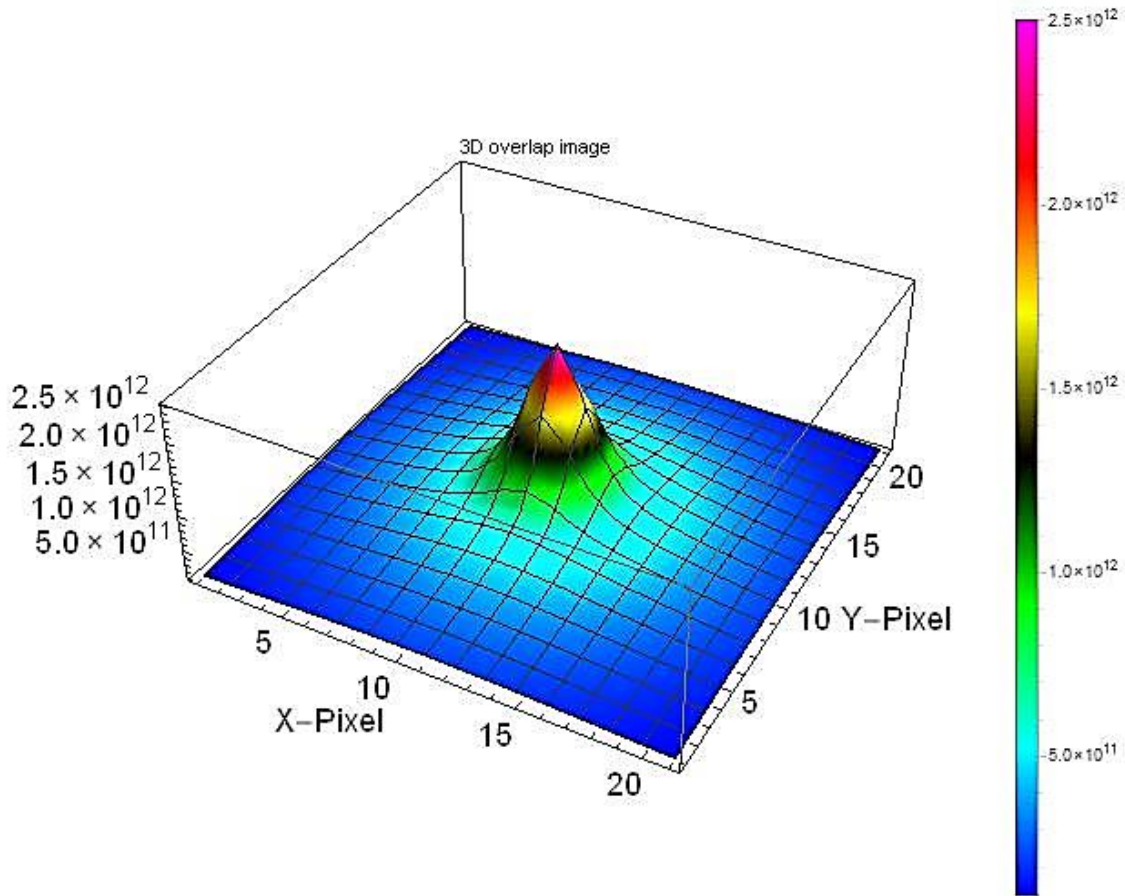
Figure 2. 13 Theoretical X-ray intensity profiles simulated from both PARMELA and measured laser parameters for the case of an unpolarized incident laser pulse.

The X-ray imaging simulation with energy dependence has been completed. The outgoing X-ray will pass through the materials, like SiO2, Be and Al, and then hit on the CsI scintillator. So, my simulation has considered their response already. All data for attenuations is from NIST XCOM program [20]. By using interpolation function via Mathematica, I combined my previous version with this to make new images with all energy response of materials. These results specifically show the *K*-edge effect.
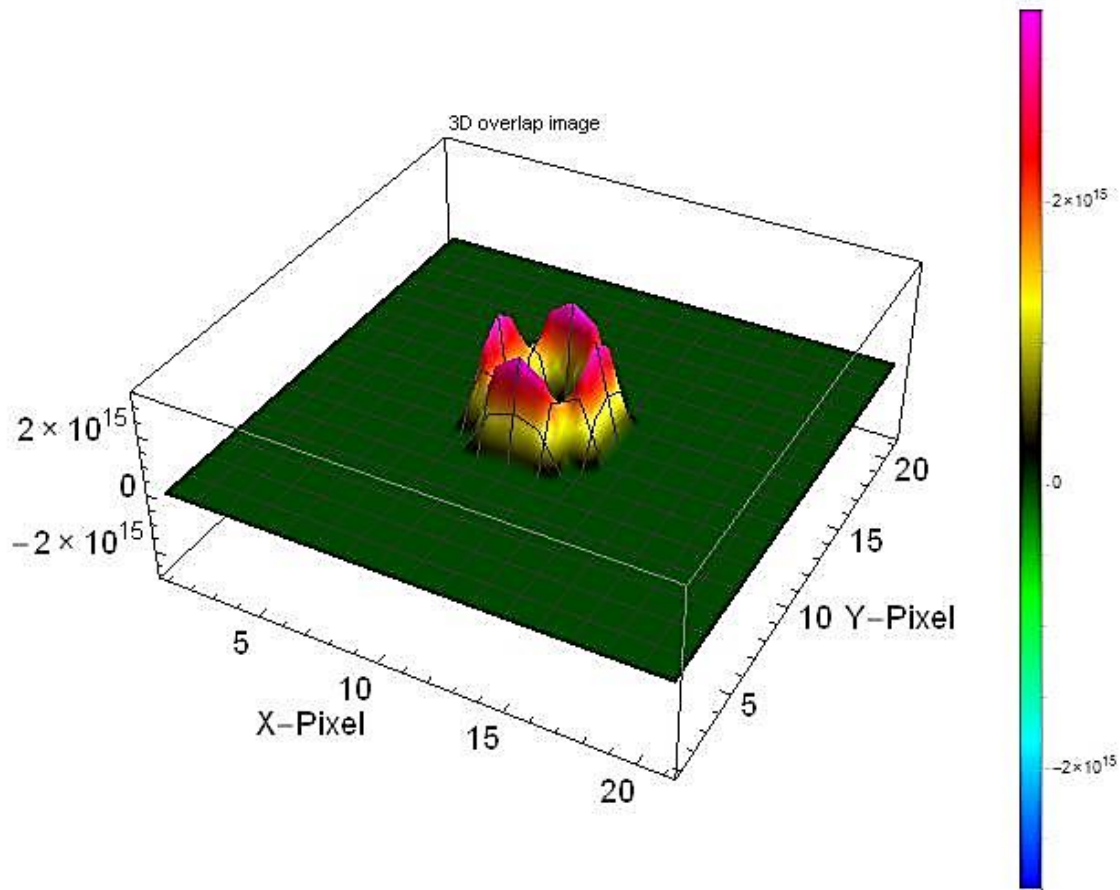
Figure 2. 14 Theoretical X-ray intensity profiles in 3D simulated from PARMELA and measured laser parameters for the case of an unpolarized laser pulse with the energy effects.

Besides, the simulations has considered the overlapping with electrons by searching for the integrated values of doses are shown below. These results are important to show how electrons act when they collide with the laser pulse. From these results, we can find the maximum intensity overall decreases. It shows that when we consider the integrated doses, the electrons are not

converted totally. Therefore, that also verifies the physical meaning of integrated dose.

Figure 2. 15 Theoretical X-ray intensity profiles in 3D simulated from PARMELA and measured laser parameters for the case of an unpolarized laser pulse with the energy effects and overlapping.
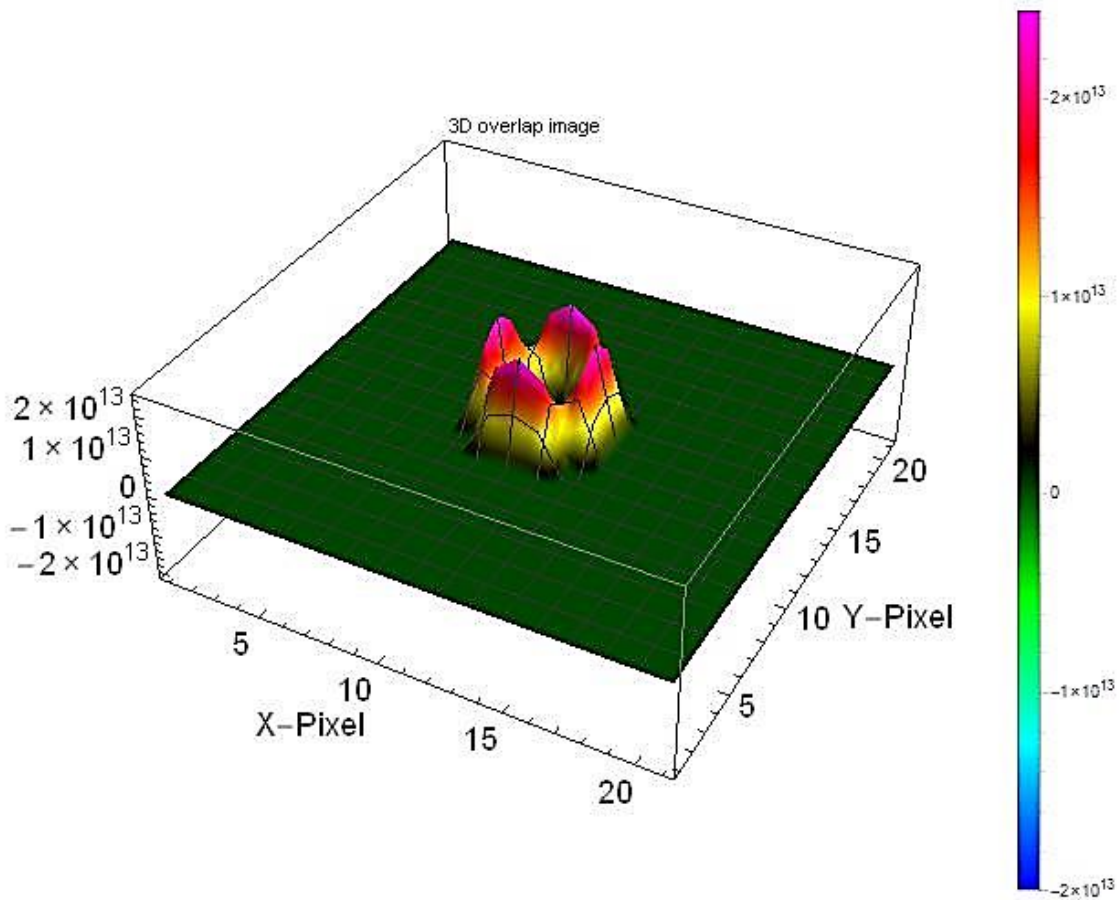

Next, X-polarized examples show that the polarization of the incoming laser does affect the interaction. These results show the images are really affected by the polarization of the laser pulse. Furthermore, the maximum intensity seems increased a little. The polarization indeed eliminates the sides along with the x-axis. That matches our expectation.

Figure 2. 16 Theoretical intensity profiles in 3D simulated from PARMELA and measured laser parameters for the case of an X-polarized laser pulse with the energy effects and overlapping.
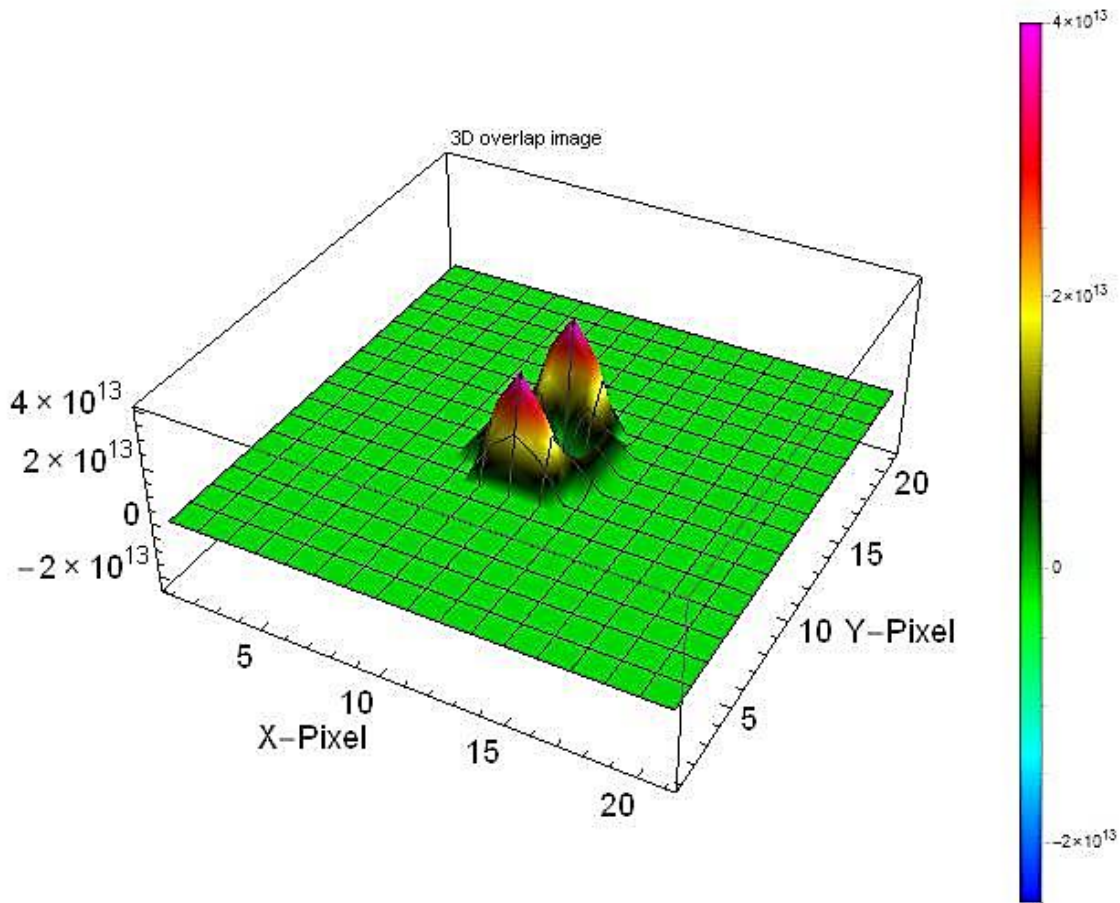
From those results, we can find out what the energy response affects the x-ray images. In addition, the overlapping does flatten the overall intensity. It is important to see how the electrons interact with the laser photons. Those results have been verified by Ref. [21].

2-5 Laguerre-Gaussian modes

We will also look to how to make a hole and explore some general properties of the interaction. One simple way to generate a beam with a hole is to use a pair of axicons (conical optics with the axis aligned along the beam direction), as shown in Figure 2.17. After the axicons, with minimal energy loss, generate a nominally collimated beam with a hole, the beam can then be focused as usual. To model the axicon effect, we used the coherent ray-tracing code FRED [22]. I have tried a few different geometries with similar results, so then we can discuss only one. We begin with a flattened Gaussian beam profile which is propagated through the axicon pair with FRED. Figure 2.18 shows the input and output radial beam profiles, showing a roughly 1 cm diameter hole in the beam. This diameter can be adjusted by changing the spacing between the two axicons. The beam was then focused with a 4 m lens. Although FRED can easily determine the beam profile at any plane after that lens, it would be helpful for integration with the Compton codes if the field at all r and z can be defined compactly. In order to do this, we decided to use a Laguerre-Gaussian beam expansion [23].
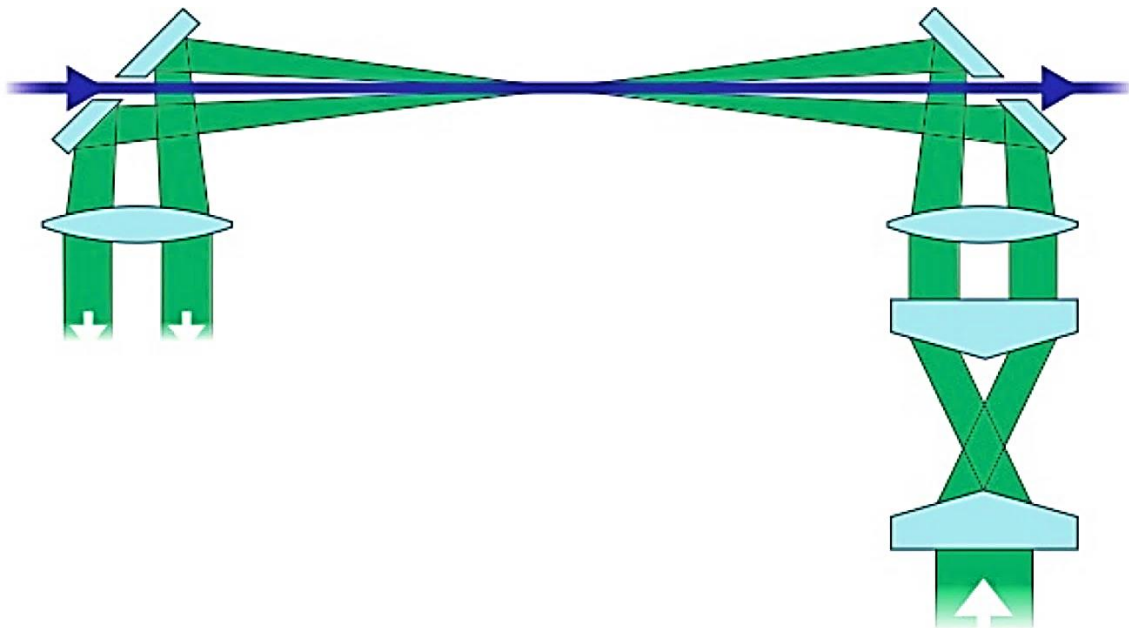
Figure 2. 17 The schematic of the insertion of laser in Compact Laser-Compton X-ray Source.
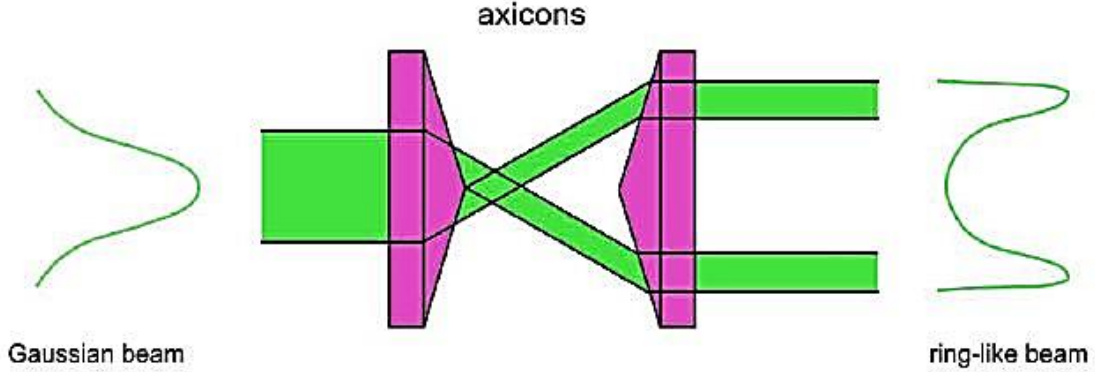
Figure 2. 18 The input and output of the axicon pair.

The Laguerre-Gaussian modes,

$$u_{pm}(r,\theta,z) = \sqrt{\frac{2p!}{\pi(m+p)!}} \frac{1}{w(z)} \left[\frac{q_0}{q_0^*} \frac{q^*(z)}{q(z)} \right]^{\frac{2p+m+1}{2}} \left(\frac{\sqrt{2}r}{w(z)} \right)^m$$

$$\times L_p^m \left(\frac{2r^2}{w(z)^2} \right) \exp\left[-ik\frac{r^2}{2q(z)} + im\theta \right] \tag{34}$$

are a complete set of solutions to the paraxial wave equation and form an orthogonal set, allowing any beam profile to be expanded as

$$u(r,\theta) = \sum_{p=0,m=0}^{\infty} c_{pm} u_{pm}(r,\theta)$$

$$c_{pm} = \int_0^\infty \int_0^{2\pi} u(r,\theta) u_{pm}(r,\theta) r d\theta dr \tag{35}$$
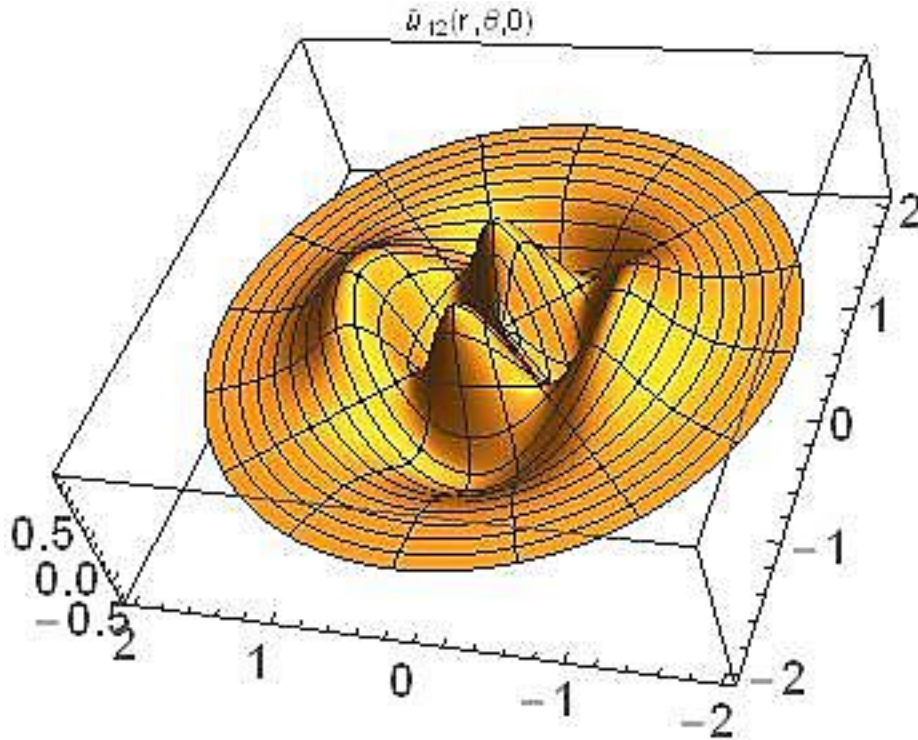
Figure 2. 19 Laguerre-Gaussian modes

In building a Compton-scattering source, one rarely has a truly Gaussian beam at the focus. In our case, we have to use a super Gaussian beam profile

$$I(r) = I_0 \exp\left(-2\left|\frac{r}{w}\right|^n\right)$$

due to the gain saturation in the Nd:YAG amplifier heads of our interaction laser, and a central obscuration in the beam due to the fact that a mirror with a hole is needed to pass the electron beam unimpeded while collecting the laser light after the interaction. We want to update these codes to enable the study of non-Gaussian beams.
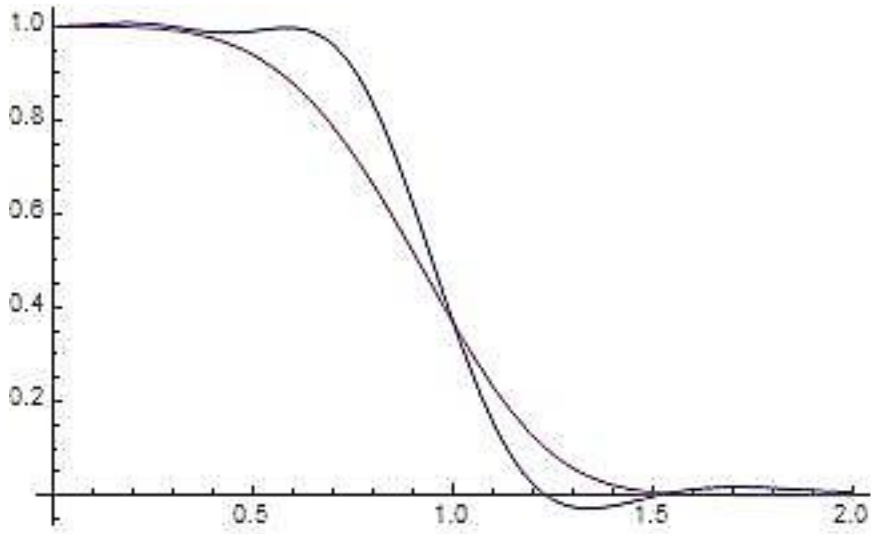
Figure 2. 20 The 2nd order supergaussian (purple) versus Laguerre-Gaussian modes (blue)
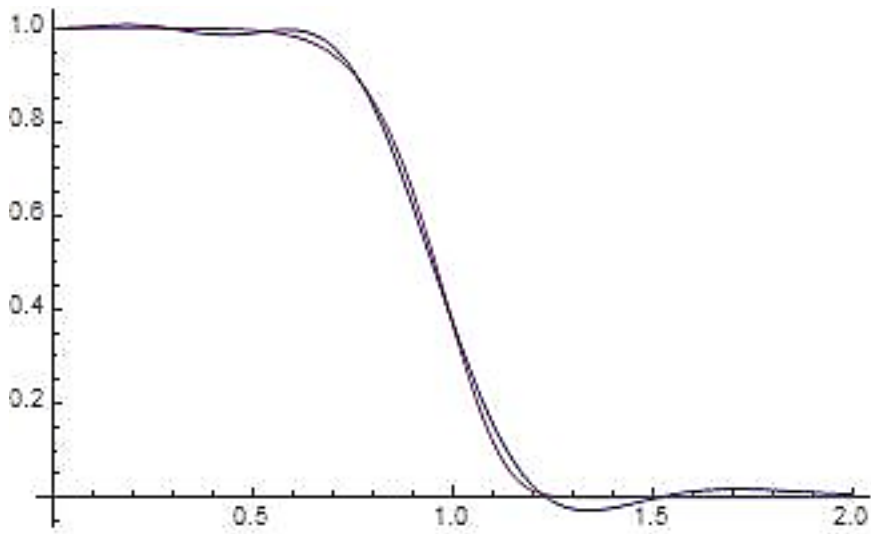
Figure 2. 21 The 4th order supergaussian (purple) versus Laguerre-Gaussian modes (blue)
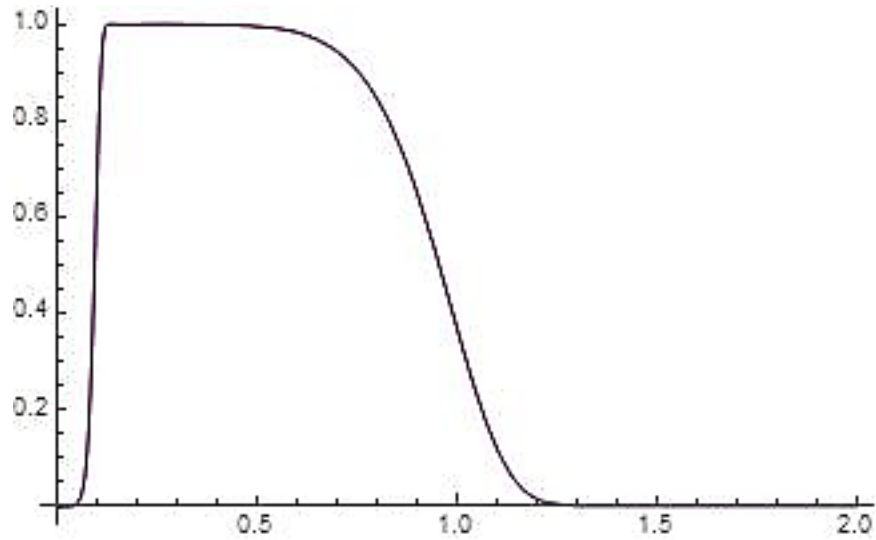
Figure 2. 22 The profile of the resultant non-Gaussian beam (i.e., Laguerre-Gaussian modes) with a desired hole.

The Figure 2.23 shows how the non-Gaussian beam propagates through the focus of the lens, which is 1500 mm. This is the important step to verify whether the non-Gaussian is appropriate. The beam should be close to Gaussian at the focus as we expected.
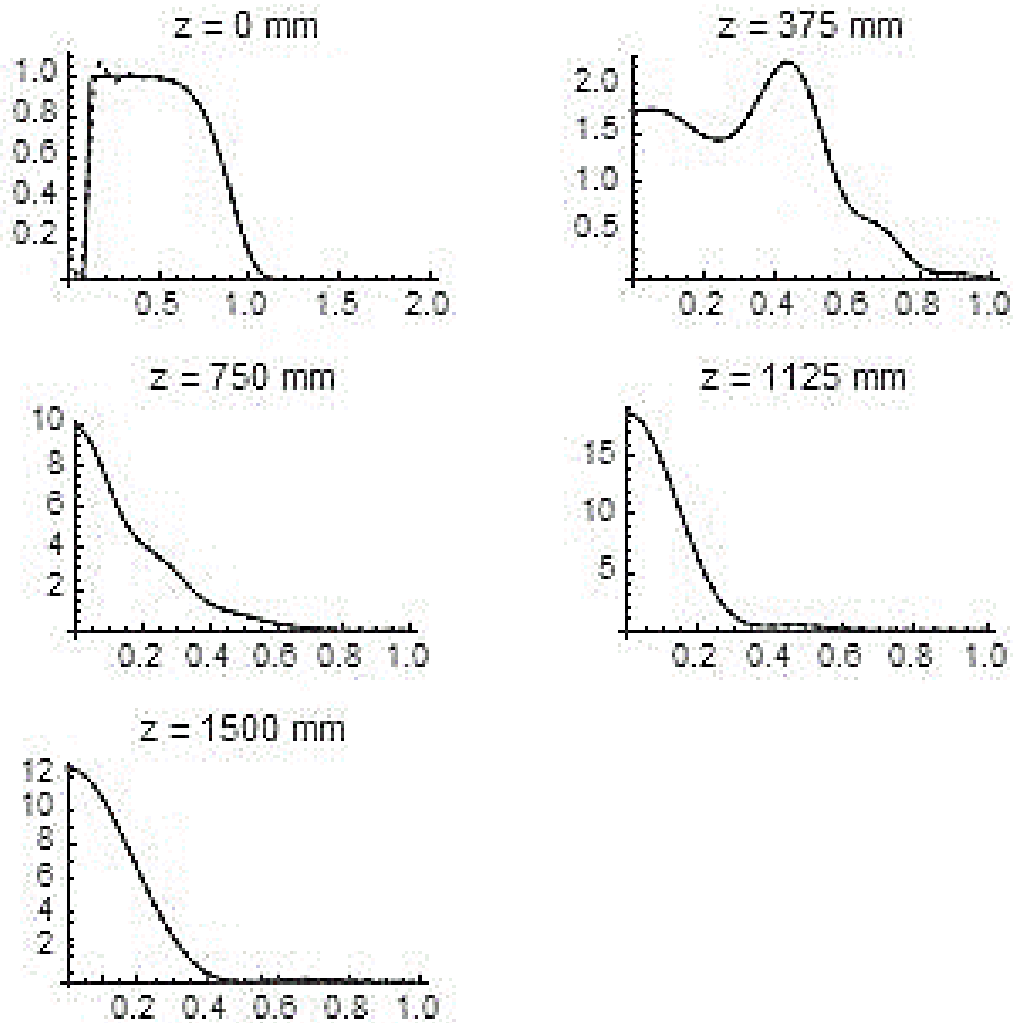
Figure 2. 23 The propagations of the resultant non-Gaussian beam (i.e., Laguerre-Gaussian modes) with a desired hole.

Now we have our need for further simulation, we can continue to substitute this beam profile into the integration in Compton code. However, the cases of Bessel beam has not been verified. Since the size of the hole will affect the beam profile itself, it is difficult to find a good match. I am still working on this project with physicists in LLNL.

2-7 Brief summary

X-ray simulation in Compact Laser-Compton X-ray Source is extremely important for the development. In order to optimize the conditions for the best output (i.e., X-ray or Gamma ray), it is better to adjust the conditions in simulation first. The next step for this work will be optimize the laser focal spot and then find out the best distribution of dose. My script is the tool to approach such goal. This work has been approved by Dr. Fred V. Hartemann and Dr. Sheldon Wu in LLNL.

Chapter 3. EXPERIMENTAL SPECTROMETER CALIBRATION

3-1 Introduction

The spectrometer of electron beams is one of the core parts of the Compact Laser-Compton X-ray Source, because it is the place for the interaction of an electron beam and a laser pulse. The design of the spectrometer is with a big magnetic dipole. To be better operate this, we have to have a completed understanding of the magnetic dipole. To correlate the energy with the deflection of an electron beam in interaction area, the profile of the magnetic dipole is necessary. Since the interaction area has to be in the vacuum chamber during operation, we need a reference field outside the chamber. The comparison between the fields inside and outside is critical for this experiment. After obtaining the data of fields, we can do the simulation for an electron beam in the chamber and calculate an output energy of an electron beam. In fact, we are using this calibration to measure energy in actual operations.
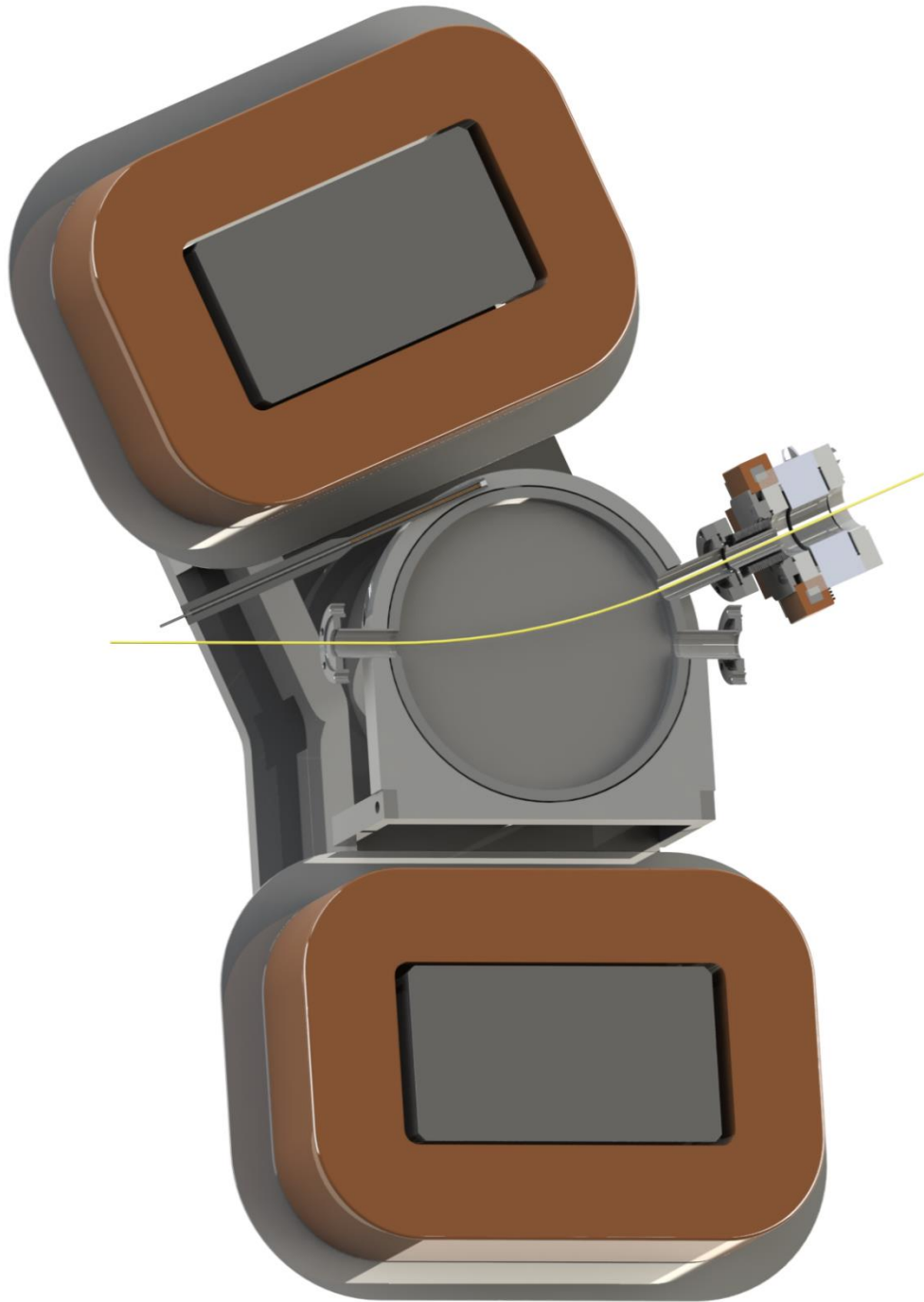
Figure 3. 1 The CAD model for the spectrometer of electron beams. The yellow line shows the path of deflecting electrons.

3-2 Experiment

To simulate the defection of an electron beam in interaction area, the profile of the magnetic dipole is necessary. The diameter of the magnetic dipole is 10.88 inches. By scanning the magnetic dipole along the path of the electron beam with the Model 460 3-channel Hall effect gaussmeter (Lake Shore Cryotronics, Inc.), the profile of the magnetic dipole shows in Figure 3.2.
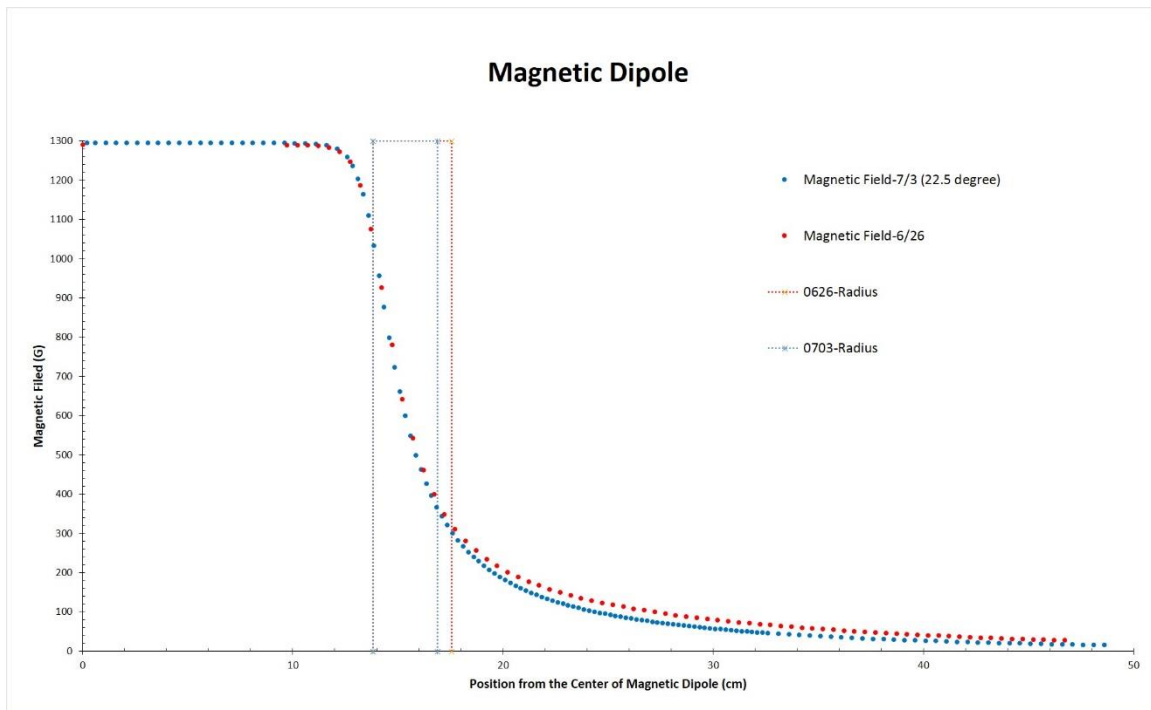
Figure 3. 2 The dipole fields from the center to the edge are measured by a gaussmeter.

As the interaction area has to be in the HV chamber during Compact Laser-Compton X-ray Source operation, it is important to obtain the reference field outside the chamber for the magnetic field in the vacuum chamber. For further use of the magnetic dipole, it demands the relation between the magnetic field of the center and the edge of the dipole. The magnetic field of

the center is measured by 3-channel gaussmeter and the one of the edge is measured by Digital Teslameter DTM-133 with MPT-132 probe (Group3 Technology Ltd.). In addition, the each voltage read with respect to the magnetic field from DTM-133 at the edge is recorded. The 0.3 and 0.6 tesla ranges are the options of interested ranges on the DTM-133 for different resolutions. By linear fitting the lines in Figure 3.3, those two equations show the relation between the magnetic field of the center and the voltage converted by the DTM-133 at the edge; then the magnetic field of the center becomes predictable.
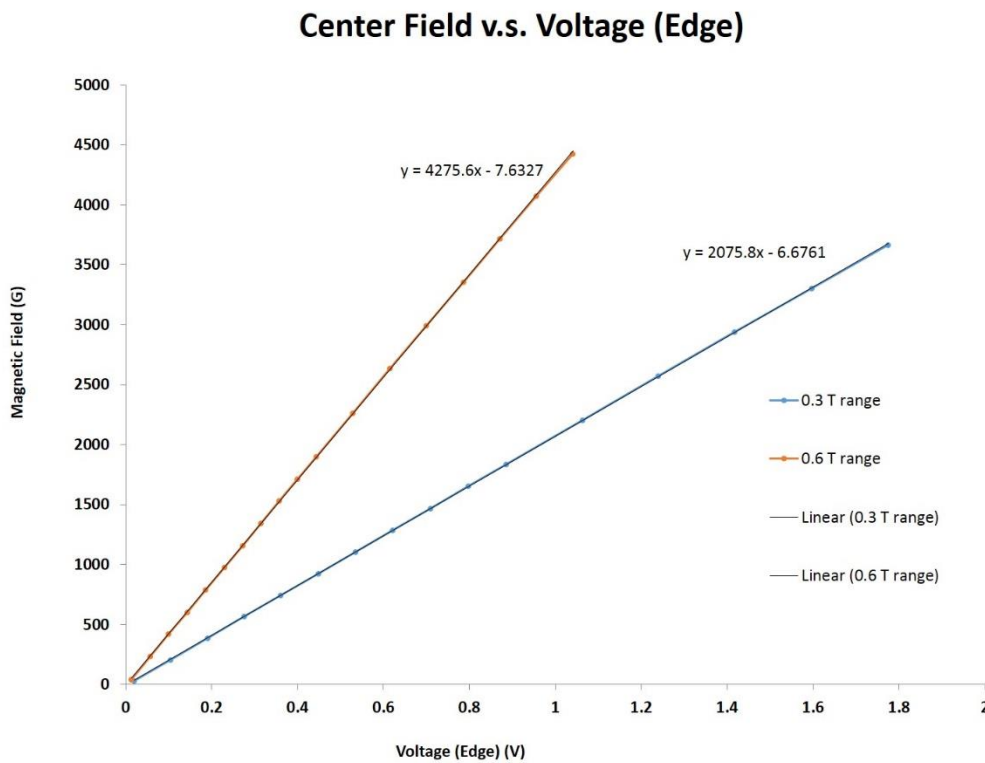
Figure 3. 3 The center field refers to the voltage read by a gaussmeter at the edge

After the above works have been carried on, the next step is to estimate the incident electron energy. The way to calculate the electron energy is based on Special Relativity in the kinetic motion of a single electron. The deflecting angle is desired as 22.5 degree. With the data of the magnetic dipole and the deflecting angle, the incident electron energy is calculated as 34.0 MeV. To understand the deflection of electron beam in vacuum chamber, it is better to simulate the moving track of the electron. The method to simulate is using the same kinetic theory in Special Relativity with parameters, like the vector of incident velocity and the magnetic field of the dipole. This simulation has two different aspects to approach. In Figure 3.4, the blue line shows the track is simulated by interpolating the data of magnetic field in dipole with quick 1-D linear interpolation in MATLAB as the input for magnetic field. However, the red dash line uses the different approach to simulate the track, in which magnetic field is set as 1296.5 Gauss (the average of peak field) and remains uniform within the effective radius of dipole. The black circle in figure 3 is the reduced size of magnetic dipole. The result turns out almost consistent, because the outward angles of two lines are mostly matched. Thus, the hypothesis of effective radius has been proven. Nevertheless, the difference between those two methods is the paths are not very close in the dipole comparing to the outwards angles. In short, it directly shows that the characterization of the magnetic dipole is needed.
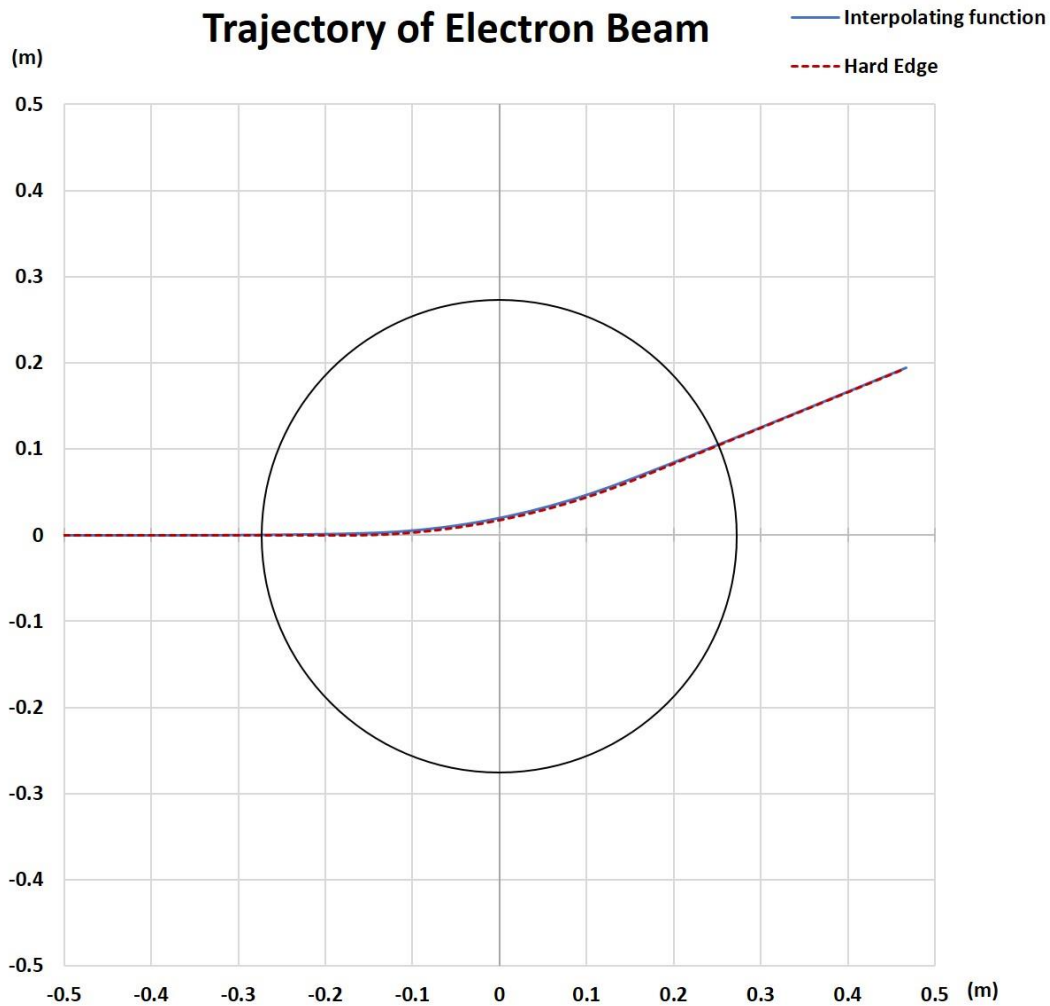
Figure 3. 4 The blue line shows the track simulated by interpolating the data of magnetic fields and the red dash line shows the path simulated by the uniform and peak field within the effective radius of dipole via MATLAB.

3-3 Brief summary

This calibration is very critical because we will not dissemble the vacuum chamber anymore. During the calibrating the spectrometer, I was very careful to not make any minor mistake, which may ruins the calibration. All

data in this experiment has been verified by physicists in the project. We were using this data for calculations and simulations for few months. No issue occurred so far. This result has been completely used in Compact Laser-Compton X-ray Source at LLNL.

Chapter 4. EXPERIMENTAL LASER FOCUS CHARATERIZATION

4-1 Introduction

Because X-rays will be generated by the interaction of an electron bunch and a laser pulse colliding head-on, the X-ray must go through an optic after the spectrometer. So, there is an oblique hole on that optic in order to allow X-ray passes through without attenuation. The purpose for a pair of axicons is that a Bessel beam (near field) and an annular ring (far field) are formed when an axicon is illuminated with a Gaussian beam. Two axicons together produce a thick-walled hollow "pipe" of light to avoid energy loss in the hole. The apex angles of the axicons in this setup are 175 degrees. Initial tests found the focal spot of a lens after a pair of axicons vanishes with axicon separation. Therefore, this experiment is to specifically study the pair of axicons in use for our laser focus.

This work can also combine with the simulation I am working on. I will have to apply all parameters I choose or adjust in this experiment into the simulation code in order to get close to the practical situation. Thus, this work is highly relevant to the simulation.
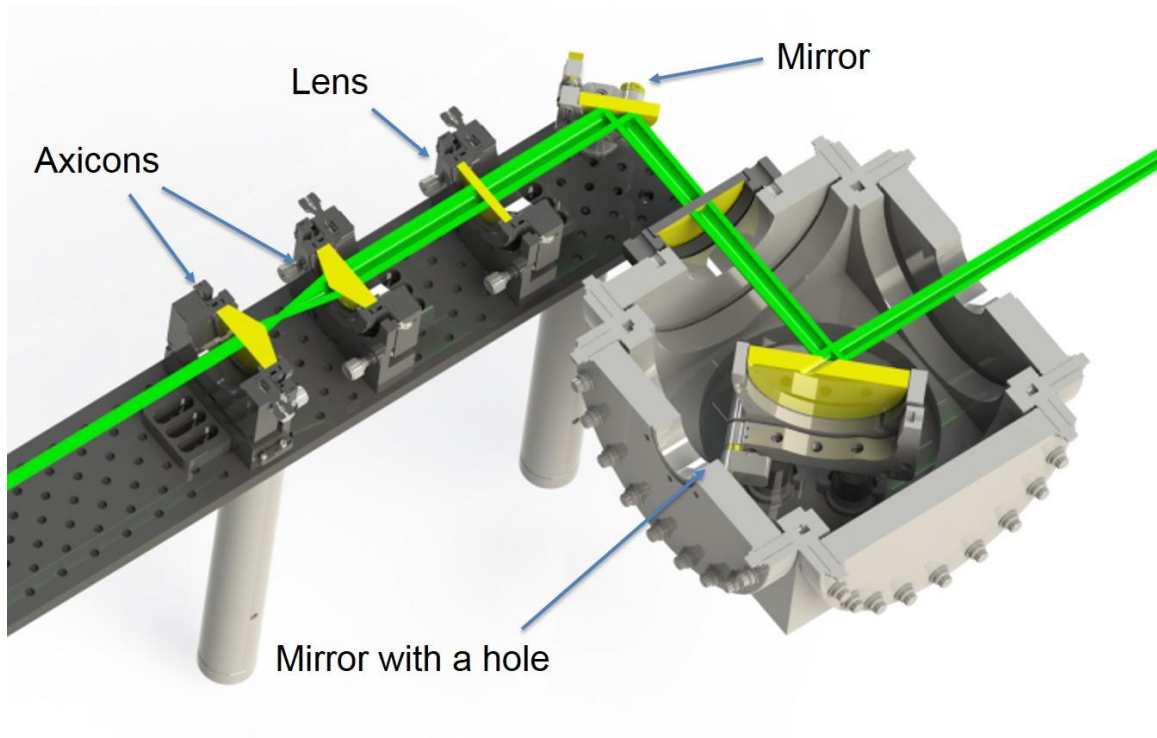
Figure 4. 1 The CAD model for actual setup in operation.

4-2 Experiment

In this optical design, we use 3mW Green He-Ne as a source to simulate the actual laser beam in Compact Laser-Compton X-ray Source. In order to simulate the size of the beam from diode-pumped Nd:YAG, we have to magnify the laser of Green He-Ne to certain scale and collimate it. Once we have done that, we can propagate the beam to the next stage, which is the pair of axicons. We set up the CCD next to the pair of axicons. The focal spot captured by the CCD is shown.
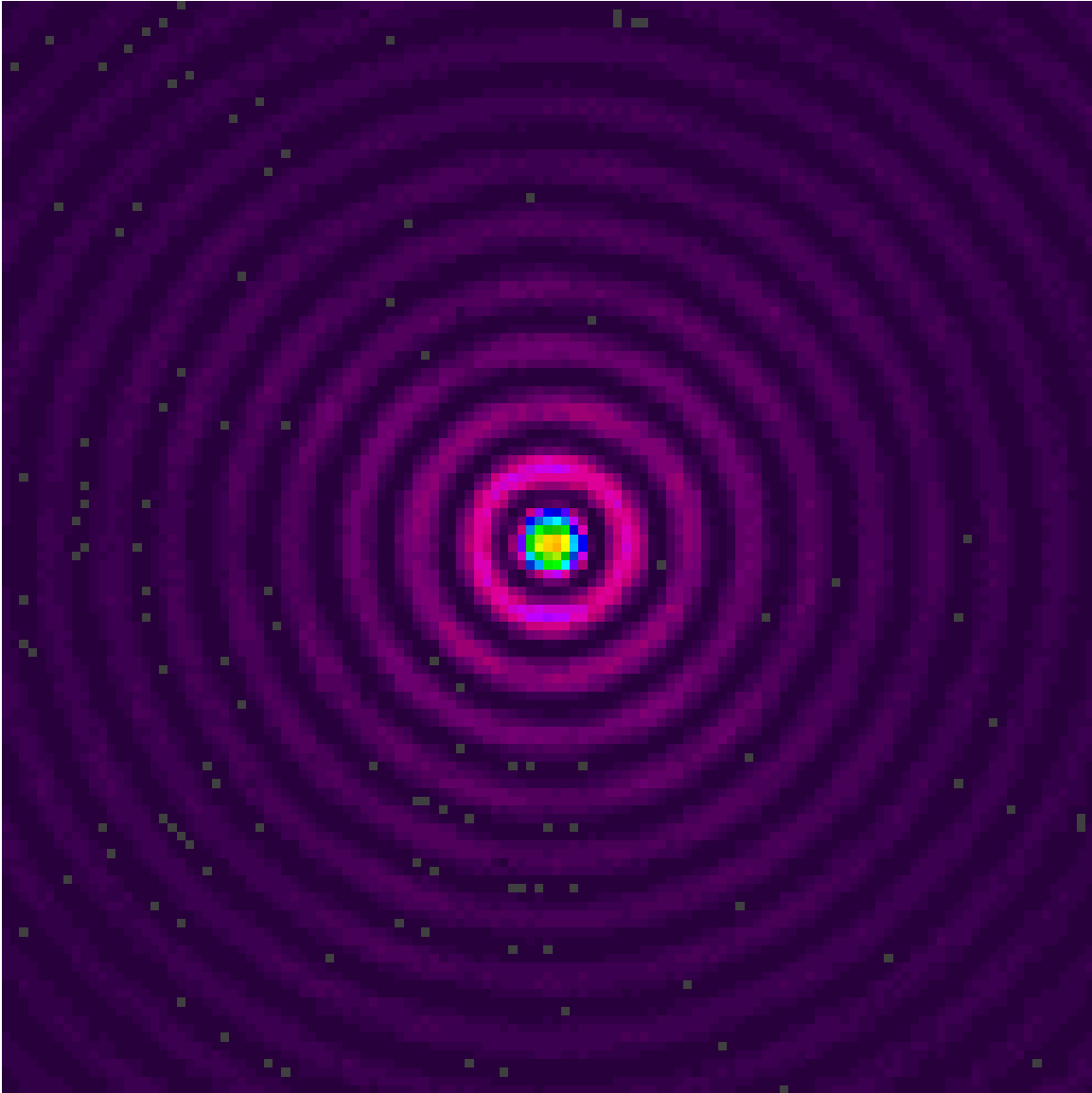
Figure 4. 2 Focal spot of Green He-Ne is detected by a camera (Spificon LW 230 CCD).

4-3 Brief summary

This experiment did simulate the size of the Nd:YAG laser. It also showed the same feature as we expected. However, the adjustment was difficult to achieve the suitable spacing between axicons. The further work will

be that we may seek for the optimized spacing between axicons via computational simulation. Therefore, the next step is that we try to do the simulation of optical tracking to resolve this problem as quick as possible. By applying the results from the simulation into the experiment, we hope we can complete the project soon. Anyway, the project is still ongoing.

Chapter 5. CONCLUSION

X-ray simulation in Compact Laser-Compton X-ray Source is extremely important for the development. In order to optimize the conditions for the best output (i.e., X-ray or Gamma ray), it is better to adjust the conditions in simulation first. The next step for this work will be optimize the laser focal spot and then find out the best distribution of dose. My script is the tool to approach such goal. This work has been approved by Dr. Fred V. Hartemann and Dr. Sheldon Wu in LLNL.

This calibration is very critical because we will not dissemble the vacuum chamber anymore. During the calibrating the spectrometer, I was very careful to not make any minor mistake, which may ruins the calibration. All data in this experiment has been verified by physicists in the project. We were using this data for calculations and simulations for few months. No issue occurred so far. This result has been completely used in Compact Laser-Compton X-ray Source at LLNL.

This experiment did simulate the size of the Nd:YAG laser. It also showed the same feature as we expected. However, the adjustment was difficult to achieve the suitable spacing between axicons. The further work will be that we may seek for the optimized spacing between axicons via computational simulation. Therefore, the next step is that we try to do the simulation of optical tracking to resolve this problem as quick as possible. By applying the results from the simulation into the experiment, we hope we can complete the project soon. Anyway, the project is still ongoing.

The overall theoretical and experimental works are successful, because they have been carried out and somewhat completed. Those research works do benefit the Compact Laser-Compton X-ray Source project. The physicists now in LLNL are still using most of my works.

The Compton-scattering systems, in which incoming high-intensity laser photons scatter off a relativistic electron beam, taking some of the

electron energy, and emerge as high-energy x-ray or γ-ray photons, have shown promise as a new class of light source, with applications from atomic [24] and to nuclear [25] [26] [27] [28] to particle physics [29] [30]. Some sources could be valuable in medical field [31].

Bibliography

[1] R. W. Schoenlein et al., "Femtosecond X-ray Pulses at 0.4 Å Generated by 90° Thomson Scattering: A Tool for Probing the Structural Dynamics of Materials," vol. 274, pp. 236-238, 1996.

[2] A. Rousse et al., "Femtosecond x-ray crystallography," *Rev. Mod. Phys.*, vol. 73, p. 17, 2001.

[3] F. Zernike, "How I Discovered Phase Contrast," *Science*, vol. 121, p. 345, 1955.

[4] E Roessl et al., "K-edge imaging in x-ray computed tomography using multi-bin photon counting detectors," *Phys. Med. Biol.*, vol. 52, p. 4679, 2007.

[5] D. Attwood, *Soft X-Rays and Extreme Ultraviolet Radiation*. Cambridge, Egnland: Cambridge University Press, 2007, ch. 5.

[6] SLAC Linac Coherent Light Source. [Online]. lcls.slac.stanford.edu/

[7] European XFEL. [Online]. http://www.xfel.eu/

[8] U. Kneissl et al., "Investigation of nuclear structure by resonance fluorescence scattering," *Prog. Part. Nucl. Phys.*, vol. 37, p. 349, 1996.

[9] P. Coleman, *Positron Beams and Their Applications*. Singapore: World Scientific, 2000.

[10] F. Albert et al., "Isotope-specific detection of low-density materials with laser-based monoenergetic gamma-rays," *Opt. Lett.*, vol. 35, no. 3, pp. 354-356, 2010.

[11] F. V. Hartemann et al., "Three-dimensional theory of emittance in Compton scattering and x-ray protein crystallography," *Phys. Rev. E*, vol. 64, no. 016501, 2001.

[12] UCLA PBPL. [Online]. http://pbpl.physics.ucla.edu/Computing/Code_Overview/#parmela

[13] F.V. Hartemann et al., "Gamma-ray Compton light source development at LLNL," in *PAC07*, Albuquerque, NM, 2007.

[14] W.J. Brown and F.V. Hartemann, "Three-dimensional time and frequency-domain theory of femtosecond x-ray pulse generation through Thomson scattering," vol. 7, no. 060703, 2004.

[15] F.V. Hartemann et al., "Overview of Mono-Energetic Gamma-ray Sources & Applications," in *IPAC 2010*, Kyoto, Japan, 2010.

[16] G. Bhatt et al., "Relativistic spin-dependent Compton scattering from electrons," *Phys. Rev. A*, pp. 28, 2195, 1983.

[17] W.E. Baylis et al., "Compton-effect Calculation for Astrophysical Application," *Zeitschrift Fur Astrophysik*, vol. 66, pp. 271-291, 1967.

[18] F. Albert et al., "Characterization and applications of a tunable, laser-based," *Phys. Rev. ST Accel. Beams*, vol. 13, no. 070704, 2010.

[19] F.V. Hartemann et al., "High-energy scaling of Compton scattering light sources," *Phys. Rev. ST Accel. Beams*, vol. 8, no. 100702, 2005.

[20] NIST XCOM. [Online]. http://www.nist.gov/pml/data/xcom/

[21] W.J. Brown et al., "Experimental characterization of an ultrafast Thomson scattering x-ray source with three-dimensional time and frequency-domain analysis," *Phys. Rev. ST Accel. Beams*, vol. 7, no. 060702, 2004.

[22] FRED Software. [Online]. http://photonengr.com/software/

[23] A. E. Siegman, *Lasers*. Sausalito, CA, USA: University Science Books, 1986.

[24] A. H. Chin et al., "Ultrafast Structural Dynamics in InSb Probed by Time-Resolved X-Ray Diffraction," *Phys. Rev. Lett.* , vol. 83, p. 336, 1999.

[25] H. R. Weller et al., "Research opportunities at the upgraded HIγS facility," *Prog. Part. Nucl. Phys.*, vol. 62, p. 257, 2009.

[26] E. C. Schreiber et al., "First measurement of the near-threshold 2H($\vec{\gamma}$,n)p analyzing power using a free-electron laser based γ-ray source," *Phys. Rev. C*, vol. 61, no. 061604, 2000.

[27] C.E. Thorn et al., "The legs electron spectrometer for tagging backscattered photons," *Nucl. Instrum. Methods Phys. Res., Sect. A*, vol. 285, p. 447, 1989.

[28] O. Bartalini et al., "Measurement of πphotoproduction on the proton from 550 to 1500 MeV at GRAAL," *Eur. Phys. J. A*, vol. 26, p. 399, 2005.

[29] T. Nakano et al., "Multi-GeV laser-electron photon project at SPring-8," *Nucl. Phys. A*, vol. 684, p. 71, 2001.

[30] M. Sumihama et al., "The γ→p→K+Λ and γ→p→K+Σ0 reactions at forward angles with photon energies from 1.5 to 2.4 GeV," *Phys. Rev. C*, vol. 73, no. 035214, 2006.

[31] F. E. Carroll et al., "Pulsed tunable monochromatic X-ray beams from a compact source: new opportunities.," *Am. J. Roentgenol*, vol. 181, p. 1197, 2003.

Vita

Po-Chun Yeh was born in Taipei City, Taiwan, on April 2, 1988, the son of Dr. Ching-Hui Yeh and Mei-Shu Hsieh. After completing his education in National Hualien Senior High School in Hualien, Taiwan in 2006, he entered the Department of Physics in National Taiwan Normal University in Taipei City, Taiwan, and received the degree of Bachelor of Science in 2010. During the following years, he was accepted as a graduate student and supported by Department of Physics and Astronomy in University of California, Irvine. He has been working at the department under Dr. Toshiki Tajima and Lawrence Livermore National Laboratory under Dr. C.P.J. Barty since 2013.

Address: 1023 Verano Place, Irvine, CA 92617

This thesis was typed by the author.